



University of Kentucky
UKnowledge

Theses and Dissertations--Physics and
Astronomy

Physics and Astronomy

2013

DEVELOPMENT OF A PATIENT SPECIFIC IMAGE PLANNING SYSTEM FOR RADIATION THERAPY

Bishnu Bahadur Thapa
University of Kentucky, bissang07@gmail.com

[Right click to open a feedback form in a new tab to let us know how this document benefits you.](#)

Recommended Citation

Thapa, Bishnu Bahadur, "DEVELOPMENT OF A PATIENT SPECIFIC IMAGE PLANNING SYSTEM FOR RADIATION THERAPY" (2013). *Theses and Dissertations--Physics and Astronomy*. 11.
https://uknowledge.uky.edu/physastron_etds/11

This Doctoral Dissertation is brought to you for free and open access by the Physics and Astronomy at UKnowledge. It has been accepted for inclusion in Theses and Dissertations--Physics and Astronomy by an authorized administrator of UKnowledge. For more information, please contact UKnowledge@lsv.uky.edu.

STUDENT AGREEMENT:

I represent that my thesis or dissertation and abstract are my original work. Proper attribution has been given to all outside sources. I understand that I am solely responsible for obtaining any needed copyright permissions. I have obtained and attached hereto needed written permission statements(s) from the owner(s) of each third-party copyrighted matter to be included in my work, allowing electronic distribution (if such use is not permitted by the fair use doctrine).

I hereby grant to The University of Kentucky and its agents the non-exclusive license to archive and make accessible my work in whole or in part in all forms of media, now or hereafter known. I agree that the document mentioned above may be made available immediately for worldwide access unless a preapproved embargo applies.

I retain all other ownership rights to the copyright of my work. I also retain the right to use in future works (such as articles or books) all or part of my work. I understand that I am free to register the copyright to my work.

REVIEW, APPROVAL AND ACCEPTANCE

The document mentioned above has been reviewed and accepted by the student's advisor, on behalf of the advisory committee, and by the Director of Graduate Studies (DGS), on behalf of the program; we verify that this is the final, approved version of the student's dissertation including all changes required by the advisory committee. The undersigned agree to abide by the statements above.

Bishnu Bahadur Thapa, Student

Dr. Janelle A. Molloy, Major Professor

Dr. Tim Gorringer, Director of Graduate Studies

DEVELOPMENT OF A PATIENT SPECIFIC IMAGE PLANNING SYSTEM FOR
RADIATION THERAPY

DISSERTATION

A dissertation submitted in partial fulfillment of the
requirements for the degree of Doctor of Philosophy in the
College of Arts and Sciences
at the University of Kentucky

By
Bishnu Bahadur Thapa

Lexington, Kentucky

Director: Dr. Janelle A. Molloy, Associate Professor of Radiation Medicine

Lexington, Kentucky

2013

Copyright © Bishnu Bahadur Thapa, 2013

ABSTRACT OF DISSERTATION

DEVELOPMENT OF A PATIENT SPECIFIC IMAGE PLANNING SYSTEM FOR RADIATION THERAPY

A patient specific image planning system (IPS) was developed that can be used to assist in kV imaging technique selection during localization for radiotherapy. The IPS algorithm performs a divergent ray-trace through a three dimensional computed tomography (CT) data set. Energy-specific attenuation through each voxel of the CT data set is calculated and imaging detector response is integrated into the algorithm to determine the absolute values of pixel intensity and image contrast. Phantom testing demonstrated that image contrast resulting from under exposure, over exposure as well as a contrast plateau can be predicted by use of a prospective image planning algorithm. Phantom data suggest the potential for reducing imaging dose by selecting a high kVp without loss of image contrast. In the clinic, image acquisition parameters can be predicted using the IPS that reduce patient dose without loss of useful image contrast.

KEYWORDS: image planning system, radiotherapy, image-guided therapy, simulation, planar imaging

Bishnu Bahadur Thapa
Student's Signature

May 28, 2013
Date

DEVELOPMENT OF A PATIENT SPECIFIC IMAGE PLANNING SYSTEM FOR
RADIATION THERAPY

By

Bishnu Bahadur Thapa

Dr. Janelle A. Molloy
Director of Dissertation

Dr. Tim Gorringer
Director of Graduate Studies

May 28, 2013
Date

To my parents:

Mr. Shayam Bahadur Thapa and Mrs. Chandra Kumari Thapa

ACKNOWLEDGMENTS

First of all, I would like to express my deepest gratitude to Dr. Janelle A. Molloy, my research advisor. Her time, patience, guidance, support and advice throughout the course of my Ph.D. have been invaluable. Dr. Molloy was always a source of inspiration and motivation as I completed this challenging journey. I very much appreciate the level of confidence she always had in me, and her willingness to listen to the little problems that cropped up in the course of research. This dissertation would not have been possible without her outstanding contribution. I cannot imagine a better advisor and mentor for my Ph.D. study.

My sincere thanks go to Dr. Kwok Wai Ng, Dr. Michael Kovash and Dr. Tim Gorringer for serving as my Ph.D. advisory committee members. Their immense professional support, constructive criticism and valuable suggestions to my dissertation are extremely appreciated. Special thanks also go to Dr. Jie Zhang for serving as my outside examiner and sharing his valuable ideas to my dissertation. For all the discussions related to my dissertation, I want to thank Dr. E. Lee Johnson, Dr. Ganesh Narayanasamy and Prakash Aryal.

I would like to acknowledge the support of the faculty and staff at the University of Kentucky Department of Radiation Medicine as well as the Department of Physics and Astronomy during my graduate study. A special thank you to Dr. Marcus E. Randall and Susan Durachta for their willingness to provide financial support from Department of Radiation Medicine. I thank Heather Russell-Simmons and Catherine Anthony for their help in editing the manuscript.

I thank my parents, Shayam Bahadur Thapa and Chandra Kumari Thapa, for their endless love, support, encouragement and patience over the years I have been away from home working towards my Ph.D. degree. I am grateful to my parents for everything they have done for me so that I could reach this point. I am also thankful to my parents-in-law, Sharad Bahadur Rayamajhi and Lal Kumari Rayamajhi, for their love, encouragements and support.

Grateful thanks also go to my sisters, Prema Thapa, Saraswati Thapa, Bhagbati Khadka and Ambika Karki. Their constant support and love has made life away from home a little bit easier. Special thanks to my brothers-in-law Ganesh Khadka, Shyam Karki and Bikram Rayamajhi for their tremendous support. Thanks to my nieces Anjali and Asmita, and my nephews Bhuwan and Bikash- I love you all.

I would like to thank my wife, Sangita Rayamajhi Thapa, for her love, patience, and encouragement. She supported me in every possible way during this entire journey and I cannot imagine completing this work without her constant support.

Grateful thanks go to my little daughters, Aayusha and Aabha, for coming into my life while I worked toward this degree. They bring so much happiness and joy into my life. Their smiling faces have been a source of great inspirational motivation to move ahead, they are a huge stress reliever during difficult moments.

TABLE OF CONTENTS

Acknowledgments	iii
Table of Contents.....	v
List of Tables	ix
List of Figures.....	x
CHAPTER 1: INTRODUCTION.....	1
1.1 Objective of the Thesis	1
1.2 Radiation Therapy	5
1.3 Digitally Reconstructed Radiograph	8
1.4 Image Guided Radiation Therapy.....	10
1.5 Equipment Used in Research Work.....	12
1.5.1 Kilovoltage source.....	13
1.5.2 Flat panel detector	13

1.6	Patient Alignment Using OBI System in Radiographic Mode	15
1.7	Computed Tomography.....	15
1.8	Structure of the Thesis	19
CHAPTER 2: THEORETICAL BACKGROUND		21
2.1	Interaction of Radiation in Matter.....	21
2.1.1	Photoelectric absorption	22
2.1.2	Compton scattering.....	25
2.1.3	Pair production.....	28
2.1.4	Rayleigh scattering	29
2.1.5	Total mass attenuation coefficient.....	31
2.2	Working Principle of Indirect Type FPD.....	34
2.3	Risk, Benefit Analysis for X-ray Imaging Procedures	37
2.4	Calculation of Imaging Dose.....	43
2.5	Mutual Information.....	47
CHAPTER 3: FEASIBILITY OF AN IMAGE PLANNING SYSTEM FOR IMAGE- GUIDED RADIATION THERAPY		50
3.1	Introduction.....	50

3.2	Methods and Materials	56
3.3	Results	62
3.4	Discussion	69
3.5	Conclusions.....	74
CHAPTER 4: PROSPECTIVE IMAGE PLANNING IN RADIATION THERAPY		
FOR OPTIMIZATION OF IMAGE QUALITY AND REDUCTION OF PATIENT		
DOSE		
4.1	Introduction.....	76
4.2	Methods and Materials	77
4.2.1	Image contrast prediction.....	77
4.2.2	Assessment of dose reduction.....	80
4.3	Results	83
4.3.1	Image contrast prediction.....	83
4.3.2	Assessment of dose reduction.....	87
4.4	Discussion	91
4.5	Conclusions.....	97
CHAPTER 5: CONCLUDING REMARKS.....		
5.1	Summary	98

5.2	Conclusions.....	101
APPENDIX	102
A. 1	List of Abbreviations	102
BIBLIOGRAPHY	105
VITA	117

LIST OF TABLES

2.1	Typical effective doses from various medical imaging procedures	38
3.1	Differences in the use of imaging procedures in the context of radiotherapy are compared to those in diagnostic imaging.....	53
4.1	Image acquisition parameters for reference image of head/neck, thorax/abdomen and pelvis sites of the anthropomorphic phantom	79
4.2	Clinical data demonstrates facilitation of imaging dose reduction.....	88
4.3	MI between reference images versus images with presets and IPS parameters separately	91
4.4	The transmitted intensity is calculated for equally weighted spectral components of a hypothetical x-ray beam. The “Full bone” calculations consider photoelectric interactions, whereas the “Water equivalent bone” calculations only consider Compton processes..	94

LIST OF FIGURES

1.1	Block diagram shows basic steps of 3-D CRT	6
1.2	Schematic diagram of ray tracing from a virtual source position through an arbitrary patient model on the imaging plane.....	9
1.3	A DRR of a pelvis is shown. The DRR was generated by a commercial treatment planning system	10
1.4	The Linac and OBI system used at University of Kentucky Radiation Medicine clinic is shown	12
1.5	Block diagram showing the principle of indirect type digital FPD	14
1.6	GE Lightspeed RT Xtra CT at University of Kentucky radiation medicine clinic	18
2.1	In a photoelectric absorption event, an incident x-ray photon collides with a low energy (in this case, K-shell) orbital electron and transfers all of its energy to the electron	23
2.2	In Compton scattering, the incident photon is scattered by a free electron at an angle ϕ . The Compton electron carries energy T in its direction of scatter θ	25
2.3	In pair production, an incident photon vanishes on its interaction with electric field of nucleus and gives rise to an electron-positron pair	28

2.4	In the Rayleigh scattering event, the incident photon scatters off the entire atom	30
2.5	Mass attenuation coefficients (Rayleigh, Compton, photoelectric, pair production and total) for soft tissue as a function of energy	32
2.6	Mass attenuation coefficients (Rayleigh, Compton, photoelectric, pair production and total) for lead as a function of energy	33
2.7	The readout process for a FPD. Blocks A through I each represent a detector element	36
3.1	The quality of an image is a function of the imaging dose received by the patient	51
3.2	Experimental setup. Respiratory phantom was placed on the Linac couch and AP projection images were acquired at 80 mAs over a wide range of exposure	58
3.3	Experimental setup. Mammography phantom was placed on top of 19 cm of acrylic slab to get the appreciable level of attenuation along different wedges of the phantom	59
3.4	Experimental setup. Abdomen phantom model 057 was placed on the Linac couch with flat face lying on the couch.....	60
3.5	Experimental setup. Abdomen phantom model 071 was placed on the Linac couch with flat face lying on the couch.....	60

3.6	The response curve of the imaging detector is shown.....	62
3.7	The absolute values of the pixel intensity across the lung nodule embedded in lung tissue are shown.....	63
3.8	The geometric appearance of the lung nodule in the respiratory phantom is a function of the exposure level and image detector saturation	65
3.9	As the image approaches saturation at high mAs values, the nodule gradually becomes less visible and its geometric dimensions vary	65
3.10	The variation in image detector response is plotted across the mammography step wedge	66
3.11	The measured image (left) and simulated image (right) of the mammography step wedge phantom is shown	67
3.12	The contrast between the vertebral body and surrounding soft tissue is shown for the two abdominal phantom models studied	68
3.13	Measured (left) and simulated (right) images are compared for two abdominal phantoms	69
3.14	An example of the use of the IPS in selecting an imaging goal is shown	71
4.1	The experimental setup. The phantom was placed on the Varian Linac couch and measured images were acquired by means of OBI system attached to the Linac	77

4.2	At 80 kVp beam quality, simulated images were generated over a range of mAs values and measured image acquired at 5 mAs was taken as reference image	80
4.3	The measured images acquired daily using the preset technique factors were used to establish normal clinical variability in image quality	81
4.4	Varian x-ray tube output measured at 150 cm SSD is shown...	82
4.5	Pelvic images of anthropomorphic phantom at 80 kVp.....	84
4.6	Variation of MI for pelvic images of the anthropomorphic phantom at (a) 80 kVp and (b) 120 kVp beam qualities as a function of mAs demonstrates the IPS's predictive capability	85
4.7	Variation of MI as a function of exposure for (a) head/neck site and (b) thorax/abdomen site of the phantom at 80 kVp beam quality	86
4.8	Comparison of the MI index between a measured reference image and a range of simulated images is shown	87
4.9	The MI index for (a) AP and (b) lateral projections of patient 1(head/ neck site) are shown	89
4.10	The MI index for (a) AP and (b) lateral projections of patient 4 (abdominal site) are shown.....	90

CHAPTER 1: INTRODUCTION

1.1 Objective of the Thesis

It has long been held in the practice of radiation therapy (RT) that imaging doses are reliably inconsequential in comparison to therapeutic doses. This assumption can no longer escape scrutiny. Conventionally, this may have been true when megavoltage (MV) portal images were acquired weekly. Even as planar kilovoltage (kV) imaging systems were integrated into the localization process, the daily doses typically received by these techniques were small. However, the application of increasingly precise methods of RT delivery has prompted the need for more aggressive use of image-guided patient position verification.

Concerns over imaging dose in RT prompted the formation of Task Group (TG) 75 of the American Association of Physicists in Medicine (AAPM).¹ In their report, they cite that the imaging dose can exceed the limit for background dose from head leakage and can increase the therapeutic dose by several percent. The report states that typical doses delivered by planar kV, fluoroscopy and real-time stereotactic radio-surgery (SRS) systems can be 3, 100 and 200 milli-gray (mGy), respectively. They add that "planar kV imaging presents the possibility of deterministic skin injury."

When considered in the context of normal tissue sparing, imaging doses can represent an even higher fractional increase in the delivered dose. For

example, an adjacent normal tissue could reasonably be expected to receive on the order of 1000 mGy from scatter and leakage from an RT treatment. The addition of several hundred mGy thus represents a 10 - 50 % increase in dose. The clinical impact of this is uncertain, and may represent a reasonable cost associated with superior patient positioning. In contrast, it may be considered an unacceptable risk that should be reduced to the degree practical. Therefore, the amount of imaging dose that RT patients receive is of concern. Regardless, the science and practice of RT will benefit from an accurate knowledge of the imaging dose received by patients.

RT delivery is relying more heavily on image guidance. Absent the ability to predict image quality and patient dose, image acquisition parameters are established via generalization, subjective estimation and trial and error. Optimally, images will be acquired using acquisition parameters that produce the least patient dose that will achieve the imaging goal. It is improbable that current practice results in this situation. The geometric precision with which RT is delivered has improved markedly over the past 10 years. Intensity modulated radiation therapy (IMRT) and stereotactic body radiotherapy (SBRT) require that target positioning be achieved with millimeter accuracy. Patient immobilization systems are imperfect in their ability to assure reproducibility and are unable to fully eliminate intra-fraction patient motion. These concerns present an imperative for aggressive image-guidance.

In many clinical scenarios, it is desirable for imaging to be performed in real time, and extend for the duration of the radiation delivery. Currently, this

practice is limited to SRS systems. However, it is likely that if imaging goals were overtly prescribed, and if the resulting patient dose were well understood, that this practice could be extended to other clinical scenarios. The lack of this information is likely limiting the use of real-time image guidance. Increased use of real-time image guidance could help alleviate concerns over discrete patient movements, as well as allow for assessment of respiratory motion. In fact, respiratory-gated and motion tracking technologies would benefit from removing their reliance on motion surrogates, such as reflective markers, that have been shown to have limited correlation with tumor motion.^{2,3}

The study of organ specific response to radiation doses produced by medical imaging suffers from limited precision. Current algorithms for assessing organ dose rely on generalized data collected from large patient populations. The dose variation across individual organs can be an order of magnitude, depending on dimensions, density and the spectral quality of the imaging beam. In current practice, the addition of imaging and therapy doses in a meaningful way is elusive. As indicated in TG 75, the regional doses delivered in RT are, by design, highly variable. Whereas in imaging applications, the doses are regionally uniform, with the exception of the indeterminate dose gradients produced by planar imaging techniques. TG75 recommends that "imaging dose should be managed on a case-by-case basis," despite the fact that there is no current precedent nor are there accurate and efficient tools with which to do so. We believe that our project takes advantage of a unique opportunity.

The patient-specific image planning system (IPS) for radiotherapy that we developed in this research work will allow RT clinicians to efficiently simulate the characteristics of planar kV x-ray images using patient-specific computed tomography (CT) scans (acquired during routine simulation). These planar images are used for patient alignment before treatment during radiotherapy. Imaging dose in terms of entrance skin exposure (ESE) will be calculated for each set of image acquisition parameters and compared to acceptable levels. By routinely calculating and reporting the dose statistics for specific organs, a large data resource will emerge. Our understanding of radiation induced co-morbidities, as well as stochastic and deterministic effects may evolve as a result of the increased data precision.

Our IPS is capable of predetermining optimal image acquisition parameters (such as kV and mAs) for a given level of patient dose and imaging goals that are valuable and achievable. For example, for scenarios in which the soft tissue tumor volume is potentially visible, as is often the case for lung tumors, imaging parameters and dose may be increased to the point of achieving minimum reliable detectability. In contrast, if low contrast object detectability is virtually impossible using reasonable imaging doses, then regional high contrast objects must be targeted for imaging with imaging doses reduced appropriately to achieve minimum reliable detectability. We expect that this will result in a paradigm shift in image-guided radiation therapy (IGRT) planning, in that the imaging goal will be overtly determined prospectively, the associated dose will be

determined prior to imaging on a patient-specific basis, and the imaging dose will always be the minimum required in order to achieve the imaging goal.

For any given patient, the outcome of the use of the IPS falls under one of the following three categories.

- The imaging dose will be reduced relative to what it would have been without the use of the system, with no loss in useful image quality.
- The imaging dose may be increased to well-defined, patient-specific predetermined levels, with an ensuing increase in useful image quality
- Real-time image guidance will be applied quantitatively, using image acquisition techniques and exposure thresholds that are prescribed and well-defined.

1.2 Radiation Therapy

RT is the use of ionizing radiation to kill cancer cells in the human body. Cell death is the result of damage to cellular DNA. The goal of RT is to kill all of the cancer cells and to spare as much surrounding normal tissue cells as possible. There are three approaches to RT:

- (1) External beam radiation: In external beam methods, the radiation beams generated outside of the patient by a linear accelerator (Linac) are focused at the tumor site.

(2) Brachytherapy: In brachytherapy, a radiation source encapsulated and sealed within a thin metallic sheath is placed inside the body close to tumor site to deliver radiation internally.

(3) Nuclear medicine: In nuclear medicine, an unsealed radiation source attached to a radiopharmaceutical or antibody is injected or taken orally to deliver radiation internally.

Among these three approaches, external beam radiation is the most common form of RT for many treatment sites. It is non-invasive and allows for sparing of normal healthy tissues and dose escalation.⁴ Three-dimensional conformal radiation therapy (3-D CRT) is used to meet the goal of RT. It is feasible only with a three-dimensional (3-D) view of the patient anatomy and a 3-D visualization of the dose distribution in the tumor and adjacent organs at risk (OARs). Figure 1.1 summarizes the basic steps of 3-DCRT.

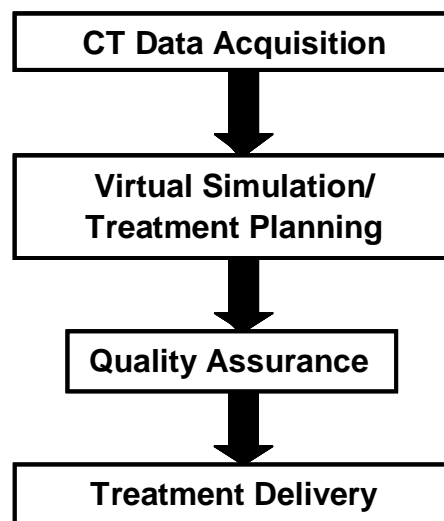


Figure 1.1: Block diagram shows basic steps of 3-D CRT.

CT was developed in the 1970s, and allowed reconstruction of the patient's anatomy in 3-D. This improved the diagnostic accuracy with which physicians could determine the location and extent of disease. However, it was not until the mid-1990s that CT 'simulation' software was developed commercially and rendered 3-DCRT delivery possible in the clinic. Two major components of a CT simulator are the CT scanner and the virtual simulation software.⁵ Simulation in RT refers to a process that defines the parameters of the patient set up and treatment geometry. In the initial phase of CT simulation, patient-specific immobilization and custom treatment devices are constructed if required. The patient is aligned on the CT simulator table in the treatment position with a three point setup technique using room lasers. Radio-opaque fiducial materials are placed on those anterior and lateral positions of the patient as external markers. The patient is then tattooed with few permanent 'pin' dots to record the position of those external markers. This allows for reproducible patient setup on the Linac prior to daily treatment. The patient is then scanned on the CT.

The patient's CT data are transferred to a powerful computer graphics workstation called a virtual simulator (VS). Virtual simulation is now built into the treatment planning system (TPS) itself. Treatment simulation of patient is carried out solely on the 3-D patient model that is created from the CT volume data of the patient. The tumor volume and organs at risk are defined directly on the CT images by a physician. The physician also places the isocenter, or focal point of the radiation beams. Radiation beam directions and radiation field shapes are

optimized by using a Beam's eye view (BEV) display. Dose calculation and final treatment plan optimization are then performed.⁶ An optimized and approved treatment plan is exported to the Linac control computer. Quality assurance (QA) of clinical treatment planning and of all equipment that are used in the course of radiation delivery is performed to ensure that the tumor is irradiated by the appropriate medical prescription dose together with minimal dose to surrounding normal tissues.^{7,8} Treatment is delivered to the patient after verifying that the patient is positioned correctly on the Linac and the beam parameters are accurately and reproducibly set. Patient positioning accuracy of ± 1 -2 millimeter (mm) can be achieved for an IMRT Linac.

1.3 Digitally Reconstructed Radiograph

A digitally reconstructed radiograph (DRR) is a fixed image of a particular beam orientation and a critical element in the process of virtual simulation. The DRR is used for patient alignment before delivering the treatment by comparing it with the image acquired by an imaging system attached to Linac.

DRRs are computer generated planar x-ray like images produced by tracing divergent ray lines from a virtual source position to a virtual plane, through the 3D patient model containing attenuation coefficient information in the form of CT numbers.^{9,10} Figure 1.2 is a schematic diagram of the spatial distribution of the transmitted intensity that impinges on the imaging plane.

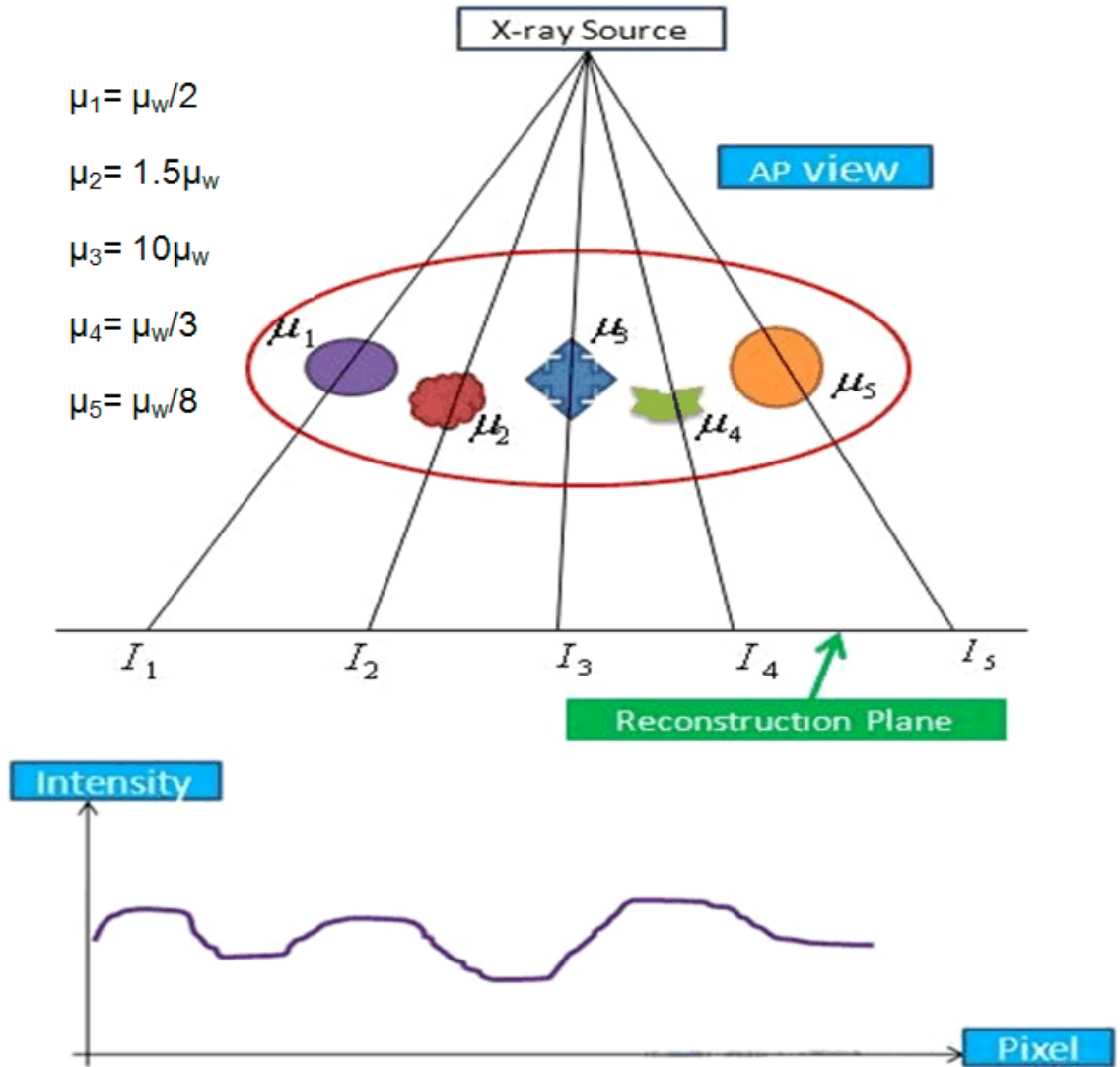


Figure 1.2: Schematic diagram of ray tracing from a virtual source position through an arbitrary patient model on the imaging plane. The sum of the attenuation coefficients along all ray lines at different positions on the imaging plane produces the spatial distribution of intensity on the imaging plane.

Figure 1.3 is a DRR of a pelvic region generated from a 3-D CT data set. The DRR was produced by a commercial TPS. A DRR serves as the reference image in evaluating the daily position of the patient. The radiation isocenter is

indicated by the plus sign, and provides an absolute reference point for spatial alignment.

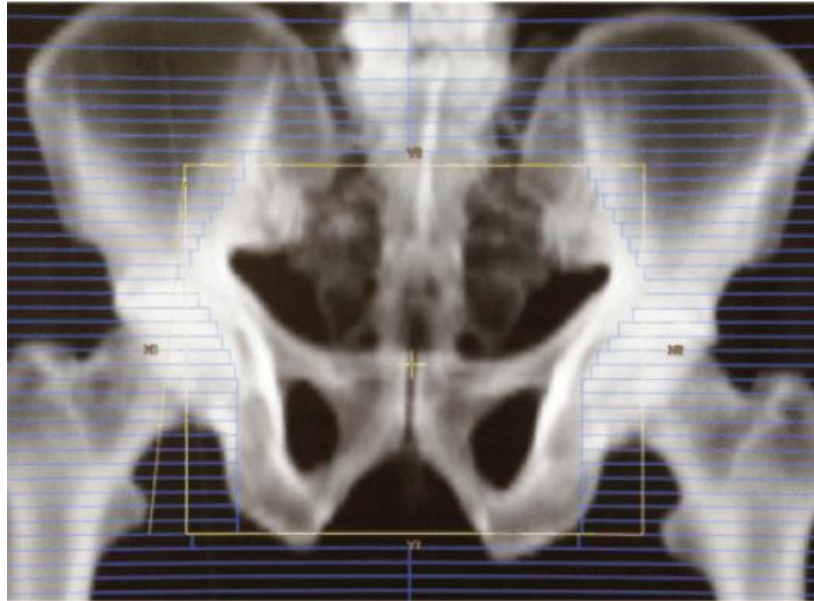


Figure 1.3: A DRR of a pelvis is shown. The DRR was generated by a commercial treatment planning system. The multi-leaf collimator (MLC) field shape and the isocenter are shown in the DRR image. Blue lines show how MLCs conform to target volume. Variations in net transmitted intensity reveal anatomical information, especially that pertaining to bony anatomy. Courtesy of M. Y. Y Law.¹¹

1.4 Image Guided Radiation Therapy

A critical step for conformal RT is accurate patient setup and target localization in the treatment position. IGRT refers to imaging performed in the treatment room immediately prior to, or during RT treatment. IGRT is an

approach for conformal radiation delivery as traditional methods like skin marks or tattoos and boney structures from port films are not very reliable for patient alignment. Because of an organ motion and changes in its anatomic shape and size during the course of the treatment, skin marks and tattoos may be problematic for patient alignment. Port films are taken at MV beam qualities, and as such there is no soft tissue contrast and even boney detail is poor, and hence may be problematic for patient alignment.

Various types of digital imaging technologies are used for IGRT with imaging devices mounted to the treatment machine or in the treatment room. With IGRT technology, the dose can be delivered precisely to the tumors by monitoring tumor motion.¹² The radiation beam can then be adjusted based on the position of the target and critical organs while the patient is in the treatment position.

Among different techniques of IGRT, a kV imaging device referred to as an on- board imager (OBI) (OBI, Varian Medical Systems, Palo Alto, CA) has been in routine clinical use in our clinic. This research work is limited only in radiographic mode of the OBI system. In the OBI system, radiographic images (referred to herein as “OBI images”) mainly reveal boney anatomy, since soft tissue is almost always indistinguishable in these images. By means of specialized computer software, these images are compared to the images taken during simulation. Necessary adjustments are then made to the patient’s position for more precise targeting of the radiation beams.

1.5 Equipment Used in Research Work

A Varian 21 Platinum (Varian Medical Systems, Palo Alto, CA) Linac in our clinic is equipped with a kV OBI system in addition to the MV electronic portal imaging device (EPID) and is shown in Figure 1.4. OBI is one of the IGRT tools in routine clinical use for RT delivery. It is a device mounted perpendicular to the treatment beam on the Linac. The OBI consists of a kV x-ray source (kVS) and a kV amorphous silicon detector (kVD) mounted on two robotic arms called ExactArms[®]. These arms can be moved along three axes of motion (i.e. laterally,



Figure 1.4: The Linac and OBI system used at University of Kentucky Radiation Medicine clinic is shown. The kVS is on the left in the figure and the kVD is opposite to it.

longitudinally and vertically). The source to detector distance is variable, but is most often set to 150 cm. The source to axis distance is 100 cm. Verification of patient position on the treatment table can be accomplished with three kV-

imaging modes: radiographic, fluoroscopic and cone-beam computed tomography (CBCT). All studies presented herein pertain to radiographic mode.

1.5.1 Kilovoltage source

The x-ray source is a Varian G242 model. It is a rotating anode x-ray tube with a tungsten/ rhenium (W-Re) target that has an inherent filtration of 0.7 mm plus an additional 2.0 mm aluminum filtration. The tube has a target angle of 14°, focal spot sizes of 0.4 and 0.8 mm, anode diameter of 100 mm, anode heat capacity of 600 kilo-heat units (kHU) and a maximum field size of 50×50 cm² at the isocenter. The source, like most imaging systems, has variable tube voltage, tube current and time settings that can be manually selected by the user. It generates photon spectra with kVp values ranging between 40 and 150 kVp in radiographic mode. It is driven by a 32 kW x-ray generator. X-ray beam collimation is produced by an assembly of a fixed primary beam aperture and an adjustable blade collimation system. Symmetric and asymmetric fields can be produced by the blade collimation system with a minimum and maximum field size of 2.5×2.5 cm² and 50×50 cm² at the isocenter.¹³

1.5.2 Flat panel detector

A FPD provides a high spatial resolution (pixel size, 100-200 µm), fast readout (0.4 s-1.5 s) and a wide dynamic range (70-100 dB).¹⁴⁻¹⁶ There are two types of FPDs in use. The indirect type involves a two-step process, in which x-

ray energy is first transformed into visible light using an x-ray scintillator material and then the light photons are converted into proportional charge by an array of millions of pixel sized photodiodes (Figure 1.5).

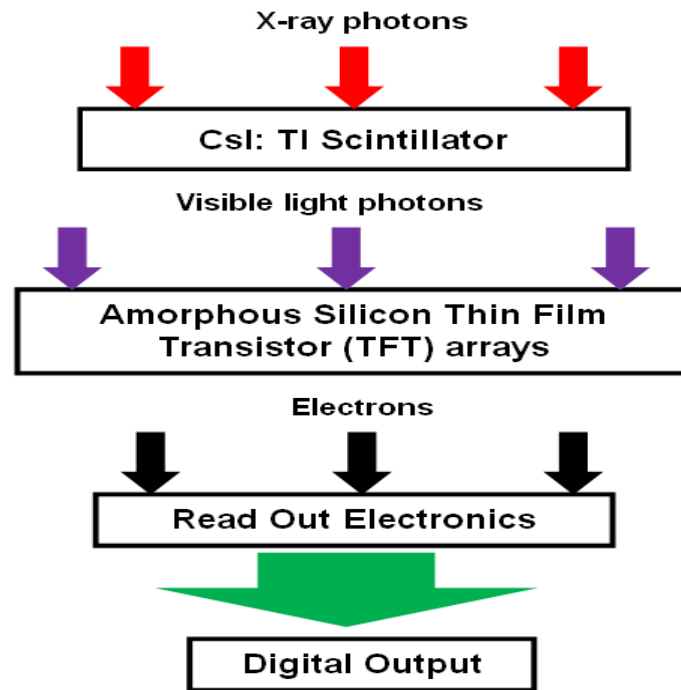


Figure 1.5: Block diagram showing the principle of indirect type digital FPD. In the first step, x-rays are converted into light photons by the scintillator phosphor material. In the second step, photodiode/transistor arrays convert light photons into electrons.

In the direct type FPD, x-rays are directly converted into charge using a semiconductor material such as amorphous selenium.¹⁷ Because of elimination of the intermediate scintillator layer, direct type FPD exhibit higher spatial resolution compared to indirect type FPD. Both indirect and direct FPDs share

the same type of readout mechanism. The working principle of the Varian OBI system uses an indirect type FPD, and is described in Chapter 2.

1.6 Patient Alignment Using OBI System in Radiographic Mode

A pair of orthogonal images is taken with the patient in treatment position. These images can be acquired at vendor-provided preset technique factors depending on the anatomical site and general size of the patient. Images can also be acquired by setting the technique factors manually. These orthogonal images are then compared to the corresponding orthogonal DRRs of the same views using the 2D2D matching software on the OBI workstation. Here, the user has the ability to compare the images using a variety of software tools including inversion effects and roving regions of interest (ROIs). The images can then be manually or automatically matched, and a suggested shift in x-, y- and z-coordinates is displayed. If this shift is accepted, the coordinates are sent to the Linac controller computer and the couch is automatically shifted prior to treatment.

1.7 Computed Tomography

CT imaging can be divided into a four step process: data acquisition, preprocessing of raw data, image reconstruction and image display. During data acquisition, the x-ray tube (and the x-ray detectors situated opposite to the x-ray

tube) rotates around the patient, who is positioned in the gantry aperture. As the radiation passes through the patient, it is attenuated by the various organs and tissues that lie in its path. The x-ray beam intensity is attenuated exponentially according to the Lambert-Beer law:¹⁸

$$I_t = I_0 e^{-\mu t} \quad (1.1)$$

where I_t is the transmitted beam intensity after the beam has passed through a thickness t of a patient, I_0 is the initial beam intensity incident on the patient and μ is the average linear attenuation coefficient along the ray. Equation (1.1) yields:

$$\mu t = \ln \left(\frac{I_0}{I_t} \right) \quad (1.2)$$

Since the ray traverses through voxels of different radiological path lengths, composition and density, the single measurement of μt can be broken up into a series of measurements.

$$\mu t = \sum_i \mu_i t_i \quad (1.3)$$

where μ_i corresponds to attenuation coefficient of i^{th} voxel that has radiological path length, t_i (i.e., product of electron density and path length corresponding to the voxel).

After preprocessing of the raw data, image reconstruction is performed using different mathematical reconstruction algorithms (e.g. filtered back projection algorithm) to convert these transmission measurements or projections into a spatial distribution of the x-ray attenuation coefficients. These values are then mapped to each voxel of the tissue into different shades of gray. Each

attenuation coefficient will be assigned a CT number (measured in Hounsfield units, HU) and hence the CT image displays CT numbers:¹⁹

$$\text{CT number} = \frac{\mu_{\text{tissue}} - \mu_{\text{water}}}{\mu_{\text{water}}} \quad (1.4)$$

where μ_{tissue} and μ_{water} correspond to the attenuation coefficient of the tissue and water respectively. The scanner is usually calibrated to result in a $\mu_{\text{water}} = 0$ HU and $\mu_{\text{air}} = -1000$ HU. The resulting image is typically a 512 x 512 matrix, or 262,144 “pixels” with 12 bits of gray scale, for a total of 4,096 shades of gray. This means that the signal in each pixel of CT image will have one of the values of HU from -1000 to + 3095.

However, human eyes cannot resolve that many shades of gray in the image but can only discern 30 to 90 shades of gray. We can change the appearance of the image by varying the window width (WW) and window level (WL). This post-processing procedure spreads a small range of CT numbers over a large range of grayscale values. This makes it easy to detect very small changes in CT number. Choice of WW and WL depends on clinical need and is user-selectable. There are also settings in which the CT image can be displayed with user definable brightness and contrast values.

In this investigation, a GE Lightspeed RT Xtra CT (GE Health, Waukesha, WI), shown in Figure 1.6 was used. It has an 80 cm wide bore and contains 16 slices. The x-ray generator kV range is from 80-140 kVp and slice thickness ranges from 0.625 to 10 mm.

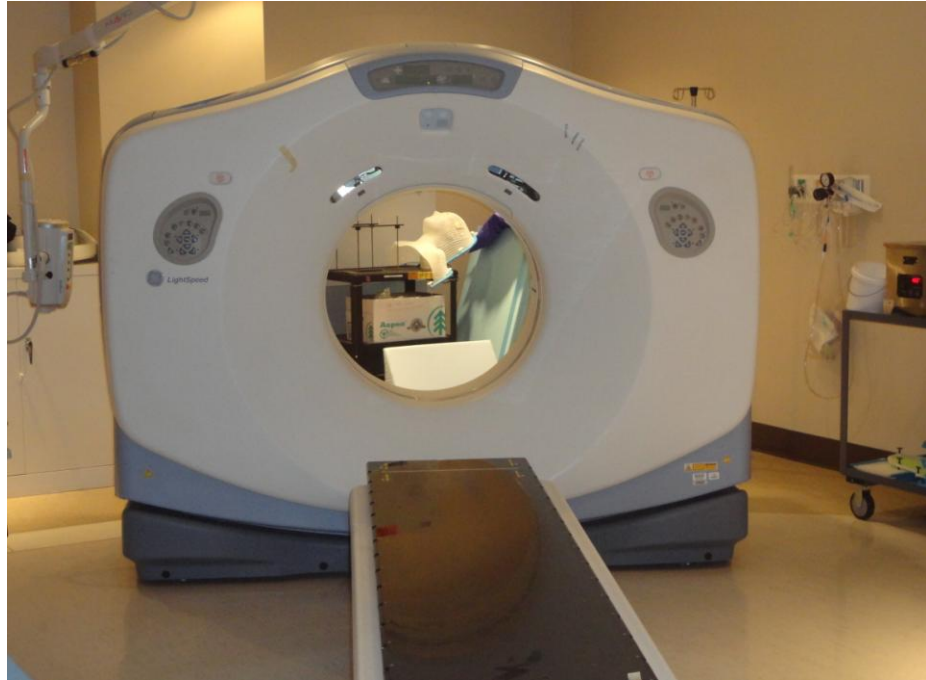


Figure 1.6: GE Lightspeed RT Xtra CT at University of Kentucky radiation medicine clinic. It was used to acquire CT images of the phantoms and the patients used in our study.

In spiral or helical CT, rotation of the x-ray source-detector assembly and table translation occur simultaneously throughout data acquisition. As such, the x-ray focus describes a helical path around the patient. A multislice helical CT scanner is equipped with a multiple-row detector array and collects data simultaneously at different slice locations. This results in faster imaging, improved longitudinal spatial resolution and better utilization of x-ray power.²⁰ Slices of different widths can be acquired by changing the beam collimation and electronically binning several detector rows together. Image quality is high and artifacts are reduced with multislice helical CT scanning.²¹

1.8 Structure of the Thesis

In this thesis, I discuss the development of a patient-specific image planning system that is capable of predetermining the optimal acquisition parameters using a common radiotherapy planar imaging chain. The IPS can be used to assist in imaging technique selection during localization for radiotherapy for a given level of patient dose and imaging goal.

The thesis consists of five chapters:

- A brief introduction to concepts relevant to issues discussed in this thesis such as DRRs, IGRT modalities, CT and our motivation for development of the IPS is given in Chapter 1.
- Chapter 2 describes the theoretical background of the types of interaction mechanisms of radiation with matter, risk benefit analysis of X- ray imaging and calculation of patient specific metrics like imaging dose resulting from different kV imaging parameters.
- The concise description of the development of an algorithm that simulates a range of image acquisition parameters and predicts the resulting image characteristics is presented in Chapter 3 along with data acquired using several test phantoms. The phantoms include a Respiratory Motion Phantom, a Mammography Step Wedge Phantom, and two Abdominal Phantoms. IPS predictive capability of small changes in contrast, image quality plateau, under and over exposure effects are established.

- Chapter 4 includes data measured with an anthropomorphic phantom which simulates human anatomy, for further justification of the IPS capability of predicting image contrast, under and over exposure effects and image quality plateau. Clinical data that show IPS capability of reducing patient imaging dose is also included.
- Chapter 5 presents the conclusions that can be drawn from chapters 3 and 4.

CHAPTER 2: THEORETICAL BACKGROUND

2.1 Interaction of Radiation in Matter

As photons are transmitted inside the body, their differential attenuation is responsible for creating the subject contrast that is encoded in the x-ray pattern that emerges from the patient. When the x-ray pattern interacts with a detector material, the subject contrast is transformed into visible image contrast, creating a two-dimensional image that can be displayed and viewed.

Photons are an indirectly ionizing radiation. They undergo a transformative event when interacting with matter that leads to a significant energy transfer to electrons. This transfer imparts energy to matter, where radiation dose is deposited.

Photoelectric absorption, Rayleigh scattering, Compton scattering and pair production are the four major types of radiation interactions with matter. The relative importance of each of these interactions depends on the incident photon energy and the atomic number of the absorbing medium. While photoelectric absorption, Rayleigh scattering and Compton scattering play a major role in diagnostic radiology,²² photoelectric absorption, Compton scattering and pair production play a major role in RT. Photonuclear and other interactions have low probability in the therapeutic energy ranges in biological matter, and do not play a significant role.

2.1.1 Photoelectric absorption

In a photoelectric interaction, the incident photon interacts with tightly bound, lower shell electron (usually the K shell) of an atom. The photon is completely absorbed and an electron, the photoelectron, is emitted with kinetic energy (E_e) equal to the photon energy ($h\nu$) minus the orbital binding energy (E_b) assuming that kinetic energy imparted to the recoiling atom is nearly zero.

$$E_e = h\nu - E_b \quad (2.1)$$

This scattered electron can produce further electron-electron ionization events, producing a large number of secondary electrons along its trail. These secondary electrons then deposit the dose locally producing biological damage.

Photoelectric interaction is followed by a subsequent cascade of electron transitions from a higher-energy orbital to fill the vacated lower-energy orbital. This results in the emission of characteristic radiation as shown in Figure 2.1, so called because its energy is characteristic of the atom's Z -value. Except in mammography, characteristic x-rays have no constructive role for x-ray imaging.

In low Z materials like soft tissue of the human body, another competing process called Auger electron emission predominates in carrying away the atomic excitation energy. In Auger electron emission, energy released because of electron transition is transferred to an orbital electron, typically in the same shell as the cascading electron.

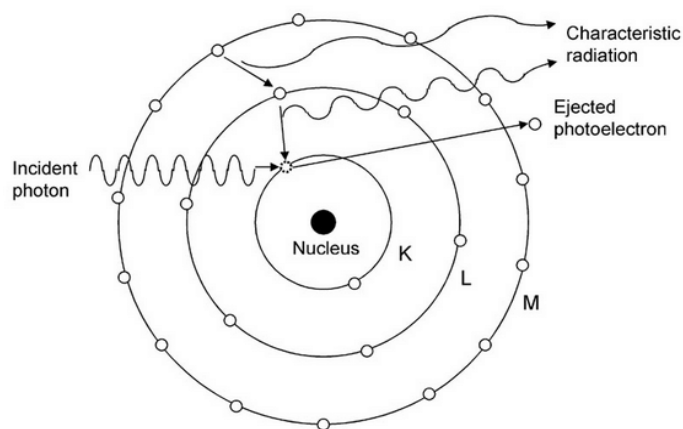


Figure 2.1: In a photoelectric absorption event, an incident x-ray photon collides with a low energy (in this case, K-shell) orbital electron and transfers all of its energy to the electron. The photoelectric event is followed by a subsequent cascade of transitions of electrons from a higher-energy orbital to fill the vacated lower-energy orbital. This results in emission of a characteristic radiation or an Auger electron.

Photoelectric effect is a first order perturbation theory calculation in which transition takes place in between an initial state (consisting of a bound electron wave function and an incident photon wave function) and a final state (consisting of a free electron wave function). The exact solutions to the equations are difficult and tedious, since the Dirac relativistic equation for a bound electron has to be used.²³ Discussion on this topic is beyond the scope of this dissertation. However, photoelectric interaction cross section per atom is found to be proportional to:

$$\tau_a \propto \frac{Z^n}{(h\nu)^m} \left(\text{cm}^2/\text{atom} \right) \quad (2.2)$$

$n \sim 4$ at $h\nu = 0.1$ MeV and gradually rises to ~ 4.6 at 3 MeV.

$m \sim 4$ at $h\nu = 0.1$ MeV and gradually rises to ~ 1 at 5 MeV.²⁴

Photoelectric interaction cross section depends on photon energy. In the keV energy range (i.e. ≤ 100 keV) where the photoelectric interaction is the most important type of interaction:

$$\tau_a \propto \frac{Z^4}{(h\nu)^3} \left(\text{cm}^2/\text{atom} \right) \quad (2.3)$$

Since number of atoms per unit mass of a material is inversely proportional to its atomic number, photoelectric mass attenuation coefficient is proportional to:

$$\frac{\tau}{\rho} \propto \left(\frac{Z}{h\nu} \right)^3 \left(\text{cm}^2/\text{g} \right) \quad (2.4)$$

Therefore, photoelectric absorption is a dominant interaction for photons used in diagnostic imaging and high atomic number materials. This explains why high contrast is possible with contrast agents (high Z materials like iodine [Z=53] and barium [Z=56]) and lower energy photons.²⁵ It also explains why x-ray detectors and shielding materials are made of high Z elements, such as gadolinium (Z=64) and lead (Z= 82), respectively.²⁶ In therapy applications the Z^3 dependence leads to significant dose deposition in tissues with high Z such as bone for superficial energy range 20-150 keV.

2.1.2 Compton scattering

In Compton scattering, the incident photon interacts with a loosely bound (nearly free) outer shell electron (of rest mass m_0) of an atom. The incident photon transfers some fraction of its energy to the electron ejecting it from the atom and gets scattered with reduced energy. As shown in Figure 2.2, the electron is scattered through an angle θ ($0 \leq \theta \leq 90^\circ$) and the photon is scattered through an angle ϕ ($0 \leq \phi \leq 180^\circ$) with respect to the original direction of the incident photon. Based on the principle of conservation of momentum and energy, kinematics of Compton interaction can be represented as:

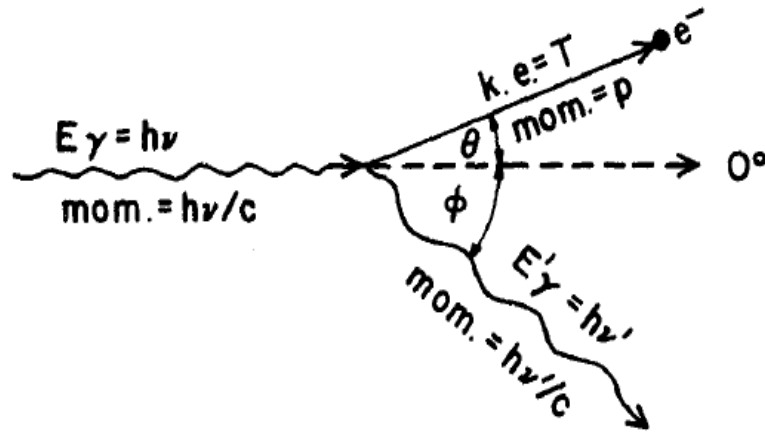


Figure 2.2: In Compton scattering, the incident photon is scattered by a free electron at an angle ϕ . The Compton electron carries energy T in its direction of scatter θ . Energy and momentum are conserved in the interaction. Courtesy of F. H. Attix.²⁷

$$h\nu' = \frac{h\nu}{1 + \frac{h\nu}{m_0c^2}(1 - \cos\phi)} \quad (2.5)$$

$$T = h\nu - h\nu' \quad (2.6)$$

$$\cot\theta = \left(1 + \frac{h\nu}{m_0c^2}\right) \tan\left(\frac{\phi}{2}\right) \quad (2.7)$$

The energy of scattered photon ($h\nu'$) becomes smaller as its scattering angle increases. The higher the incident photon energy ($h\nu$), the lower the energy of the scattered photon. At very low photon energies (~ 5 keV), photons get backscattered whereas at higher photon energies (~ 60 keV), scattering of photons is more forward peaked.^{28,29}

The electron-photon interaction in Compton scattering can be fully explained within the theory of Quantum Electrodynamics. The Klein-Nishina law gives a differential cross section for photon scattering at a given angle per unit solid angle and per unit electron using relativistic concepts. The integral of the differential cross section over all solid angles (i.e. over all possible photon scattering angles from 0 to 180 degrees) yields the total K-N cross-section per electron.³⁰

$$\sigma_e = 2\pi r_0^2 \left\{ \frac{1+\alpha}{\alpha^2} \left[\frac{2(1+\alpha)}{1+2\alpha} - \frac{\ln(1+2\alpha)}{\alpha} \right] + \frac{\ln(1+2\alpha)}{2\alpha} - \frac{1+3\alpha}{(1+2\alpha)^2} \right\} \left(\frac{\text{cm}^2}{e} \right) \quad (2.8)$$

$$\text{Here, } \alpha = \frac{h\nu(\text{MeV})}{0.511 \text{ MeV}} \quad (2.9)$$

So the K-N cross section per atom of atomic number Z is:

$$\sigma_a = Z \cdot e^\sigma \left(\text{cm}^2/\text{atom} \right) \quad (2.10)$$

Since e^σ is independent of Z , the Compton cross section per atom is proportional to Z .

$$\text{i.e. } \sigma_a \propto Z \left(\text{cm}^2/\text{atom} \right) \quad (2.11)$$

Therefore, Compton mass attenuation coefficient $\left(\frac{\sigma}{\rho} \right)$ is independent of Z .

Since the Compton interaction occurs with free electrons of the medium, the probability of this interaction is proportional to the electron density. Therefore, hydrogenous materials have almost twice the probability of Compton scattering compared to other nonhydrogenous materials. In the diagnostic x-ray energy range (10-150 keV). Compton scatter probability is independent of energy whereas at higher energies, it is inversely proportional to energy.³¹

Compton scattering predominates in soft tissues in the energy spectrum as low as 26 keV. In the diagnostic energy range used in medical applications, Compton scattering predominates over photoelectric absorption in most human tissues.³² Since the randomly scattered photons that reach an image receptor produce noise to the image, Compton interactions lower the contrast in the image. The scattered Compton electron is mainly responsible for ionization events and therefore responsible for biological damage as it traverses through the matter. The scattered photon on the other hand can interact again with an orbital electron at another location. The energy deposition pattern is, therefore, more diffuse.

2.1.3 Pair production

Pair production is an interaction between an incident photon and electric field of a nucleus. In this interaction, the photon loses all of its energy and an electron (e^-)–positron (e^+) pair is produced. The threshold energy for pair production is 1.02 MeV, the rest mass energy equivalent of two electrons. The kinetic energy shared by a pair is the difference between the incident photon energy and the threshold energy for pair production.

$$E_{e^-} + E_{e^+} = h\nu - 1.02 \text{ (MeV)} \quad (2.12)$$

The nucleus recoils to conserve momentum. The pair has significant range and is responsible for the ionization, and therefore responsible for the associated biological damage that occurs. When the positron comes to rest, it annihilates with another electron in the medium liberating two oppositely directed 0.511 MeV photons as shown in Figure 2.3.

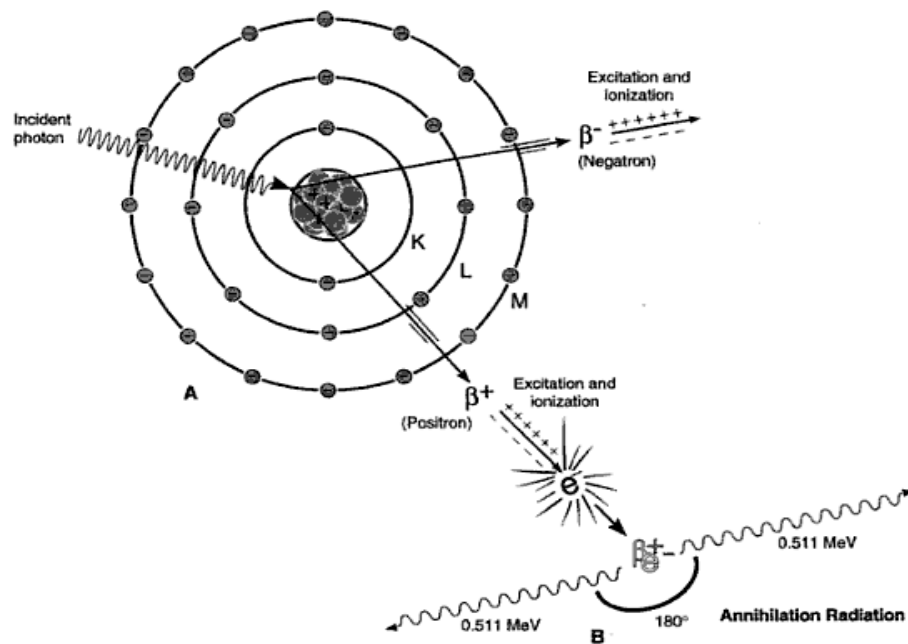


Figure 2.3: In pair production, an incident photon vanishes on its interaction with electric field of nucleus and gives rise to an electron-positron pair. Positron comes to rest after traversing a short distance in a medium and then annihilates with electron producing two 0.511 MeV photons. Courtesy of J.T. Bushberg et. al.³³

Pair production cross-section per atom is proportional to:³⁴

$$\kappa_a \propto Z^2 \left(\text{cm}^2/\text{atom} \right) \quad (2.13)$$

So the mass attenuation coefficient for pair production is:

$$\frac{\kappa}{\rho} \propto Z \left(\text{cm}^2/\text{g} \right) \quad (2.14)$$

Because of the threshold energy requirement, pair production has no role in diagnostic x-ray imaging. But at the high energy used in RT, the pair produced in the interaction has significant range and is responsible for the ionization, and therefore associated with the biological damage that occurs. The annihilation photons can undergo other interactions and hence have diffuse pattern of energy deposition.

2.1.4 Rayleigh scattering

In Rayleigh scattering, the incident x-ray photon interacts with an entire atom. When the atom's electron cloud returns to ground state energy level, a photon of the equal energy but in a slightly different direction is emitted as shown in Figure

2.4. Scattered photons mostly traverse in forward direction, also known as coherent or elastic scattering.³⁵

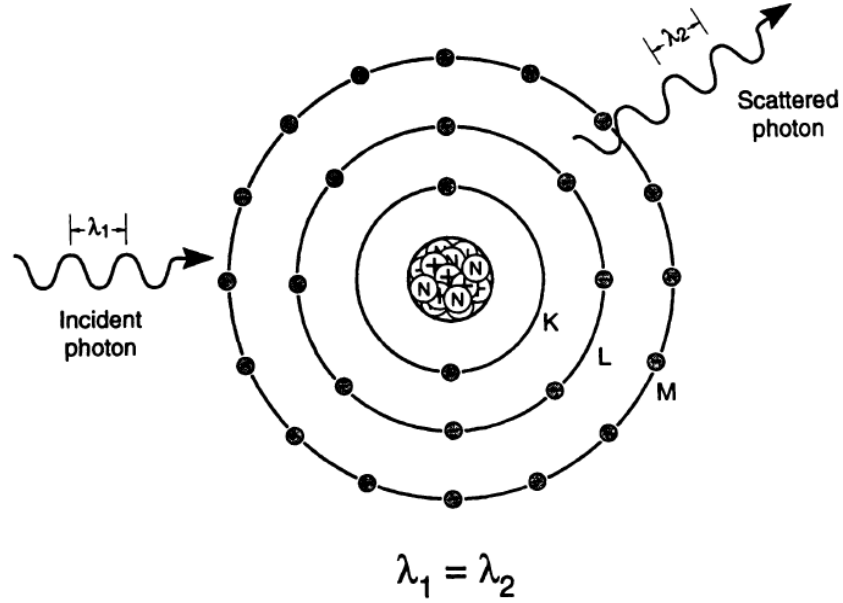


Figure 2.4: In the Rayleigh scattering event, the incident photon scatters off the entire atom. Since the energy of the scattered radiation is the same as the incident radiation, this is also called coherent scattering. Courtesy from J.T. Bushberg et. al.³⁶

Rayleigh cross-section per atom is:³⁷

$$\sigma_{a,R} \propto \left(\frac{Z}{h\nu} \right)^2 \left(\text{cm}^2/\text{atom} \right) \quad (2.15)$$

Therefore, the Rayleigh mass attenuation coefficient is:

$$\frac{\sigma_R}{\rho} \propto \frac{Z}{(h\nu)^2} \left(\text{cm}^2/\text{g} \right) \quad (2.16)$$

The probability of this interaction increases with increasing Z of the medium and decreasing energy of incident x-ray. This occurs only with very low energy diagnostic x-rays (e.g. mammography). The probability of this interaction in soft tissues for diagnostic energy used in medical applications is very low (~ 5 %). Since no energy is transferred to the medium, Rayleigh scattering plays no role in dose deposition.³⁸

2.1.5 Total mass attenuation coefficient

The total mass attenuation coefficient is a linear sum of all contributions from photoelectric absorption, Compton scattering, pair production and Rayleigh scattering (neglecting photonuclear interactions), and is given by:³⁹

$$\frac{\mu}{\rho} = \frac{\tau}{\rho} + \frac{\sigma}{\rho} + \frac{\kappa}{\rho} + \frac{\sigma_R}{\rho} \quad (2.17)$$

Figure 2.5 shows photoelectric, Compton, pair production, Rayleigh and total mass attenuation coefficients for low Z material, soft tissue (effective atomic number ~7). Photoelectric interaction is dominant only at the low energy spectrum (<26 keV). It rapidly drops off with an increase in energy. Compton interaction is dominant throughout most of the energy spectrum in soft tissue. Only at energy greater than 1.02 MeV, does pair production contribute to attenuation. Rayleigh contribution to attenuation is very small in the low energy spectrum.³⁵

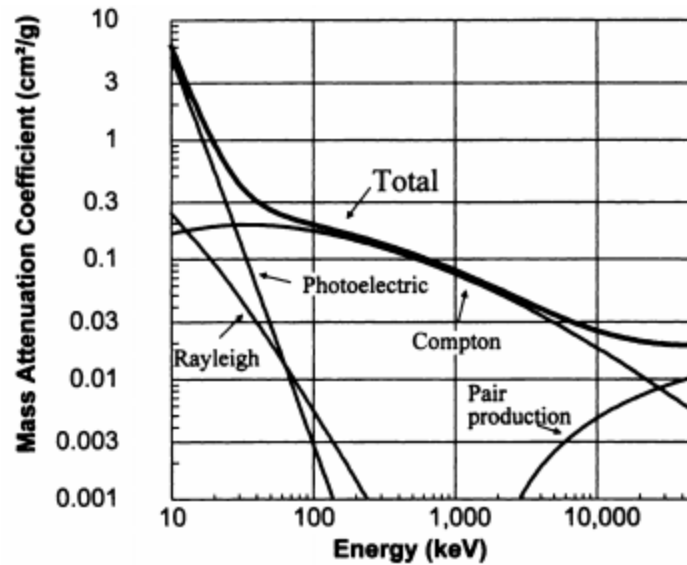


Figure 2.5: Mass attenuation coefficients (Rayleigh, Compton, photoelectric, pair production and total) for soft tissue as a function of energy. Courtesy of J.T. Bushberg et. al.⁴⁰

Figure 2.6 shows the mass attenuation coefficients for lead. Though Compton interactions also decrease with energy, this effect is more pronounced with photoelectric interaction. Abrupt increases in attenuation for lead occur at the L- edge and K-edge absorption discontinuities of 13-16 keV and 88 keV respectively.⁴¹ When the photon energy (88-90 keV) is just above the K shell binding energy (88 keV), the probability of photoelectric absorption increases for two reasons. First, a small increment comes from an increase in the number of electrons (from 80 to 82) available for the interaction. Second, a large increment comes from a resonance phenomenon that results in a disproportionately large number of K shell interactions.

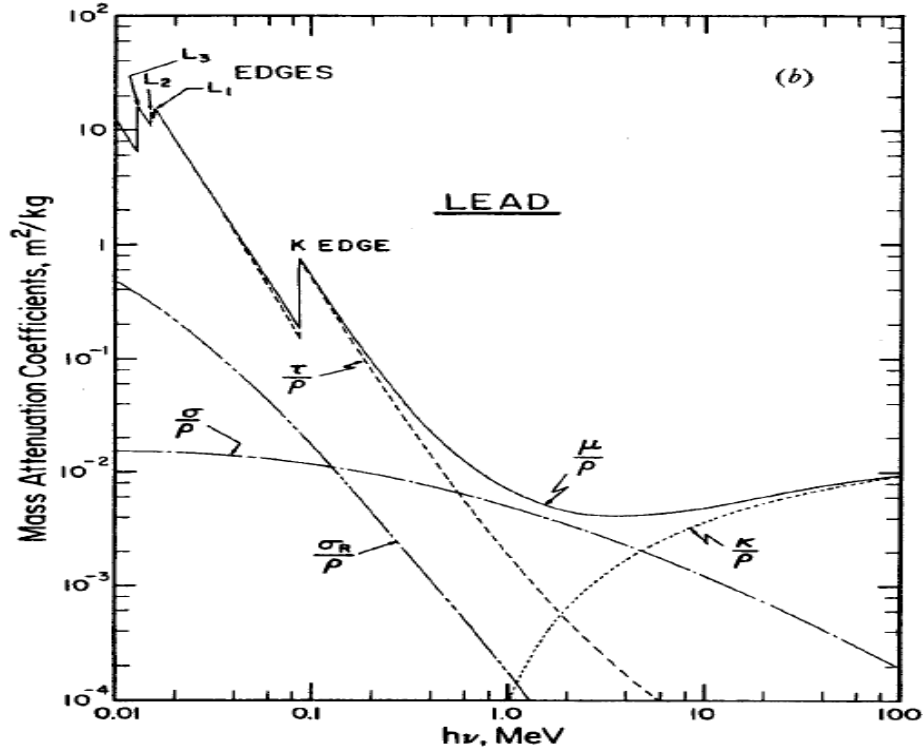


Figure 2.6: Mass attenuation coefficients (Rayleigh, Compton, photoelectric, pair production and total) for lead as a function of energy. Courtesy of F. H. Attix.⁴²

In the diagnostic energy range, two interactions are responsible for attenuating the radiation: photoelectric and Compton. Because of the Z^3 dependence, photoelectric absorption can produce better contrast between tissues with slightly different atomic numbers, such as in the case of mammography. Photoelectric absorption is dominant when diagnostic energy photons interact with high Z materials like contrast agents, bone, lead and screen phosphors. However, in cases of lower atomic number materials like tissue and air, Compton interactions dominate in diagnostic energy range. At the intermediate energy range (60 keV - 2 MeV), Compton interaction is the dominant mode of interaction for all types of materials.

2.2 Working Principle of Indirect Type FPD

FPD consists of a two dimensional array of millions of independent, pixel-size amorphous silicon (aSi) photodiodes and thin-film transistors (TFTs) deposited on a single glass substrate. aSi photodiodes are 'n-i-p' types such that the bottom layer is electron rich, the middle layer is intrinsic and the top layer is hole rich.⁴³ Each TFT acts essentially as a switch to access the associated photodiode making up an individual detector element. The source terminal of the TFT is the capacitor that stores the charge accumulated during exposure, the drain of the TFT is connected to the readout line and the gate terminal is connected to the horizontal wires called gate lines. The conductive state of the TFT is controlled through the applied voltage. Negative voltage applied to the gate causes the switch to be turned off, whereas a positive voltage applied to the gate causes the switch to turn on.⁴⁴

Layers of aSi, various metals and insulators are deposited on a single glass substrate utilizing the thin film technology to form the photodiodes, TFTs matrix, the interconnections, and the contacts on the edges of panel. Since the bulk part of FPD consists of aSi TFT arrays, it is also called TFT image receptors.⁴⁵

A uniform layer of thallium-doped cesium iodide scintillator is deposited directly on top of the aSi structure. Since the structured phosphor provides good absorption efficiency and good resolution, the phosphor is grown in very thin needles on the array.

The thallium doped cesium iodide (CsI:TI) scintillator first absorbs x-ray photons and converts them into light photons. These photons then channel toward an array of photodiodes where they are converted into electrons. During image acquisition, a negative voltage is applied to the gate lines during exposure, causing all of the transistor switches on the FPD to go to an off state and allowing charge accumulation.

During readout, switches for all detector elements along a row are turned on by applying positive voltage to each gate line, one gate line at a time. The multiplexer sequentially connects each vertical wire to the digitizer by means of switches. Each detector element along each row⁴⁶ is read out (Figure 2.7). Then the charge from each detector element is digitized by the analog to digital converter attached to each column, forming a digital image. The FPD only requires a number of electronic channels equal to the number of columns of the array.¹²

Each detector element of the FPD has a light sensitive region (called a photoconductor), and a small corner of it contains the electronics (e.g., the switch, capacitor, etc.). The fraction of the light-sensitive area relative to the entire area of the detector element is called the fill factor. Large detector elements have a high fill factor resulting in high contrast. Conversely high spatial resolution can be obtained with small detector elements.⁴⁷ Because of this, there is a tradeoff between contrast resolution and spatial resolution in choosing the detector elements size.

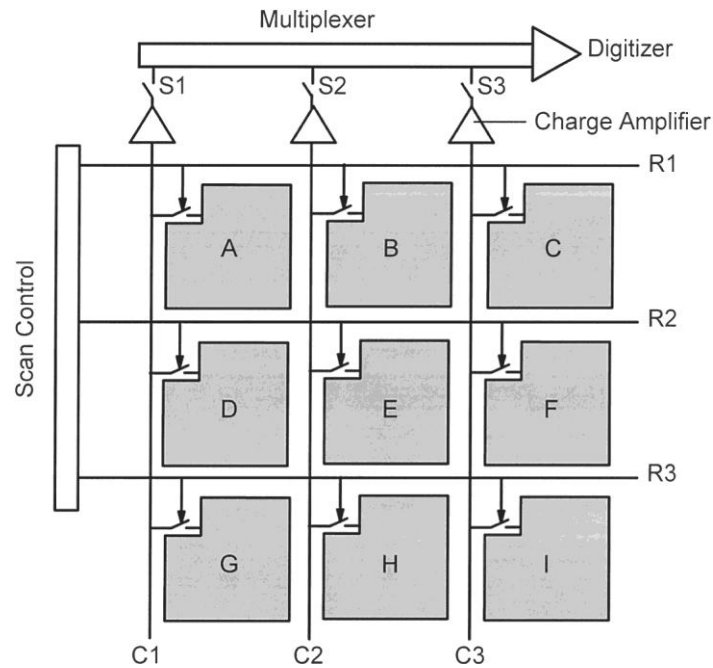


Figure 2.7: The readout process for a FPD. Blocks A through I each represent a detector element. Rows R1 through R3 each represent a gate line. Columns C1 through C3 each represent a readout line. The FPD only requires a number of electronic channels equal to the number of columns of the array. Courtesy of J.T. Bushberg et. al.⁴⁸

An aSi flat panel (model PaxScan 4030CB) of the Varian OBI device has an active rectangular imaging area of 397 mm x 298 mm. The pixel matrix size can be varied by grouping detector units together. This is called binning. The OBI system has a flat-panel detector with a matrix dimension of 1024x768 (i.e. 2x2 binning mode) producing 1024x768 resolution images. It has a pixel pitch of 194 μm (i.e. 194 μm per pixel resolution) and a fill factor of 70%.⁴⁹

2.3 Risk, Benefit Analysis for X-ray Imaging Procedures

Medical imaging methods can be broadly categorized as either using ionizing or non-ionizing techniques. Each of the imaging modalities uses different forms of energy, interacts with different human tissues in different ways and correspondingly provides different kinds of anatomic and physiologic information about them. Medical imaging is not only limited to the diagnosis of diseases, it has evolved into a tool for intra-operative navigation, radiotherapy planning, tracking of organ motion during radiation delivery, surgical planning, and tracking the progress of disease.

In the United States, the average American receives the effective doses of 3mSv per year due to exposure to ionizing radiation from different medical procedures.⁵⁰ The average effective doses of radiation from select diagnostic medical procedures are listed in Table 2.1.^{51–54} Exact doses to individuals may differ largely from these typical numbers according to the image acquisition parameters used in imaging modality based on the individual's body size and shape, as well as other factors.

CT involves larger radiation doses than the more common, conventional x-ray imaging procedures, making CT the largest contributor of medical radiation exposure to patients in most parts of the world. Although CT accounts for only 11% of all x-ray based examinations in the United States, it contributes 66 % of the total diagnostic dose delivered to patients.⁵⁵ Since the use of CT is growing

exponentially because of its diversity in several applications, imaging dose is also escalating proportionally.⁵⁶

Table 2.1: Typical effective doses from various medical imaging procedures.

Diagnostic procedure	Average effective dose in mSv
Chest radiography	0.2
Abdomen radiography	0.7
Pelvic radiography	0.6
Skull radiography	0.1
Mammography	0.4
CT chest	7.0
CT abdomen	8.0
CT pulmonary angiography	15.0
CT pelvis	4.0
CT coronary angiography	16
CT brain	2.0
Lumbar spine radiograph	1.5
Barium enema exam	8.0

Radiation dose presents two potential health hazards: stochastic and deterministic effects. These radiogenic effects result from direct and indirect interactions that damage DNA. In a direct interaction, damage occurs when a photoelectric or Compton electron ionizes a DNA molecule. In an indirect attack, hydroxyl (OH) free radicals are liberated by ionization of water molecules in the cells. These radicals may trigger DNA strand breaks or modify purine and pyrimidine bases of DNA, leading to cell death.⁵⁷

Deterministic injury such as skin burns, fibrosis and cataracts occur with high doses because the radiation kills a large number of cells. These effects manifest only above a certain threshold dose that depends on the type of radiation, health state of the individual, tissue type and biological end point. The severity of damage increases with dose.

Stochastic effects, such as late health hazards like radiation induced cancer and genetic errors, arise from exposure to low dose radiation. Stochastic effects have no dose threshold because damage to a few or even a single somatic or germ cells can produce radiogenic cancer and heritable genetic errors. While the probability of occurrence of this type of effect is proportional to dose, its severity is independent of dose.⁵⁸⁻⁶⁰

The dose from imaging procedures mainly poses the threat of stochastic risks. In few instances of prolonged interventional fluoroscopic procedures, deterministic injury was also observed.⁶¹ The International Commission on Radiological Protection (ICRP) estimates that the probability of induction of a stochastic radiogenic cancer is 5 % Sv⁻¹, as a rule of thumb.^{50,62}

Infants and children are of greatest concern regarding stochastic risks. Cells in younger people are rapidly dividing and therefore are more radiosensitive and less effective at repairing the damage caused by ionizing radiation. Younger people also have a longer life expectancy and hence, a greater probability of occurrence of radiogenic cancer. The unfortunate practice of using the same machine settings for imaging children and adults results in a large dose of

radiation for children. This is a particularly important concern during CT scanning.^{63,64}

Similarly, use of diagnostic imaging (particularly of abdomen and pelvis) in pregnant women is an important issue as it may cause radiation-induced teratogenic effects on the fetus (e.g. smaller head or brain size, abnormally slow growth, and mental retardation). Depending on the stage of pregnancy at the time of irradiation and amount of radiation dose received, the potential risks include prenatal death, intrauterine growth restriction, small head size, mental retardation, organ malformation, childhood cancer, and the occurrence of hereditary effects in the descendants.^{65–68}

Therefore, x-ray based medical imaging involves trade-offs between the benefits of accurate diagnosis and the low-probability of radiation-induced risks. It should be carried out only when the benefits outweigh the potential risks.

Non-ionizing radiation imaging techniques are the best option for children and pregnant women as they eliminate the burden of radiation risks. In routine x-ray imaging, a high contrast image can be created by decreasing kVp applied across the x-ray tube and increasing mAs for image acquisition which results in high imaging dose to patients.^{69–71} When imaging with ionizing radiation is necessary, potential imaging dose risks can be reduced by using less radiation to create the image which has the contrast just enough for diagnostic purpose.

In x-ray based imaging techniques, the subject contrast among different objects is due to differential attenuation. The dominant mode of interaction in

most imaging modalities is Compton scattering (photoelectric is dominant in mammography), and the attenuation coefficient is higher at low kV energies.^{72,73} This results in greater contrast among different tissue types at lower kVp settings.

If a small fraction of photons reach the detector, noise will dominate the image and the borders between different contrast regions become indistinguishable. Image noise can be decreased by increasing detector signal-to-noise ratio (SNR) at higher mAs values for a given kVp.⁷⁴ But in this case, dose deposited to the tissues will be high.

Image only has to be clinically adequate to make a reliable diagnosis so there will be no need for repeated imaging as a result of poor quality image. Image does not need to be the best quality at the cost of high dose.⁷⁵ Imaging dose should be kept as low as possible without losing essential imaging information, adhering to the principle of ALARA (as low as reasonably achievable).

The need for CT exams should be scrutinized before the imaging of children and pregnant women.^{76–78} Standardized optimal operating procedures should be integrated in different radiological examinations to reduce the imaging dose and hence the associated risks.^{79–81}

IGRT uses kV or MV x-ray imaging modalities as a tool for patient positioning, target localization and beam placement during external beam radiation therapy (EBRT). During RT treatment, patients are exposed to very high

and localized doses of radiation. Since IGRT procedures add a small imaging dose to the high therapeutic dose, this imaging dose has been neglected in most cases. Though small, each IGRT modality contributes dose to the patient which may be high over the course of fractionated treatment. This imaging dose also has associated risk, mostly stochastic risks of long-term induction of cancer and possible hereditary effects.^{82,83} There is a need to adhere to modern radiation protection regulations for imaging in radiotherapy such as practicing ALARA. In imaging procedures for IGRT, the conformal dose delivered to tumor, sparing surrounding normal tissue, should outweigh the potential stochastic risks. Increased imaging dose during IGRT significantly improves patient positioning, target localization and external beam alignment in radiotherapy and hence can reduce dose to healthy tissue.

An imaging dose in IGRT should be optimized so as to have a low overall concomitant dose to healthy tissue around the tumor site region and also minimizing diagnostic dose elsewhere. The AAPM TG 75 explains the management of imaging dose during image guided radiotherapy. This group recommends that management of imaging dose during radiotherapy should be done differently than during routine diagnostic imaging. This report suggests three steps for this: 1) assessment of total imaging dose to the patient, 2) reduction of that dose by refining imaging technique and 3) optimization of imaging regimen with consideration of cost/benefit analysis of imaging versus therapy dose.¹

2.4 Calculation of Imaging Dose

Measurement of radiation doses to patients is needed for biological risk assessment. Air kerma is the kinetic energy transferred to the secondary charged particle (i.e. electrons) liberated by an x-ray beam per unit mass of air. In the case of diagnostic x-rays, all the energy transferred to kinetic energy of secondary electrons is absorbed locally since the range of secondary electrons is very short in diagnostic energy range. Charged particle equilibrium exists with diagnostic x-ray photons in air and hence air kerma comes out to be equal to absorbed dose.⁸⁴ So, planar kV imaging dose is evaluated traditionally as entrance skin dose.⁸⁵

MV imaging dose is quantified in absorbed dose, which has units of J/kg or Gy. As the range of secondary electrons is too large at MV energies, air kerma and absorbed dose are not the same. So unlike in kilovoltage imaging, air kerma cannot be considered the indicator of the associated biological risk from exposure to MV imaging.¹

For CT imaging, dose is most often quantified as the CT dose index (CTDI) (in mGy).^{86,87} It is computed by the integral of the absorbed dose profile, $D(z)$, at a position z along the axis of rotation of the scanner, for a single slice, divided by the total z -direction beam width, $N \times T$ (where N is the number of slices per tube rotation and T is the acquisition slice thickness).⁸⁸

$$CTDI = \frac{1}{N T} \int_{-\infty}^{+\infty} D(z) dz \quad (2.18)$$

In practice, $CTDI_{100}$ is measured using a 100 mm long pencil ionization chamber and it represents the accumulated dose at the center of a single slice of an axial scan over a profile length of 100 mm.⁸⁹

$$CTDI_{100} = \frac{1}{N T} \int_{-50 \text{ mm}}^{+50 \text{ mm}} D(z) dz \quad (2.19)$$

In general, CTDI measurements are made by inserting the CT ionization chamber at the center and at eight equally spaced peripheral positions of a cylindrical acrylic phantom. $CTDI_w$, the weighted average of these $CTDI_{100}$ measurements represents the average radiation dose to the patient.

$$CTDI_w = \frac{2}{3} CTDI_{100} (\text{periphery}) + \frac{1}{3} CTDI_{100} (\text{center}) \quad (2.20)$$

For helical scans at a pitch p , “volume CTDI” is introduced as a correction of the $CTDI_w$ due to the overlap or gap between scans as determined by the pitch.⁹⁰

$$CTDI_{vol} = \frac{CTDI_w}{p} \quad (2.21)$$

Dose length product (DLP) represents integrated dose.⁹¹

$$DLP = L \times CTDI_{vol} \quad (2.22)$$

where L is total z-direction length of the examination.

If deterministic detriments are likely, as reported in the literature from prolonged fluoroscopically guided interventional procedures, the risk is evaluated at the entrance using units of Gy.^{92,93} On the other hand, effective dose is the standard dose descriptor of the stochastic radiation risk for the induction of cancer and the induction of genetic effects in the offspring of individuals exposed

to ionizing radiation. Effective dose (E) is used as a metric for comparison of the stochastic detriment associated with different diagnostic radiologic procedures.⁹⁴ Effective dose as defined by Jacobi⁹⁵ is “the mean absorbed dose from a uniform whole body irradiation that results in the same total radiation detriment as from the non-uniform, partial-body irradiation in question”.

ICRP- 60 defines effective dose (E) as:⁹⁶

$$E = \sum_T w_T H_T \quad (2.23)$$

where the H_T are the average doses to tissue T for a particular exam, and the w_T are tissue weighting factors that represent the relative radiation sensitivities of that tissue. So, effective dose is the weighted summation of the absorbed dose to each specified tissue multiplied by the ICRP- defined tissue-weighting factor for that tissue. Stochastic risk is expressed in Sieverts (Sv). The ICRP- 60 probability coefficient of fatal cancer risk is $5.0 \times 10^{-2} \text{ Sv}^{-1}$. This coefficient is based on the linear no- threshold (LNT) model of radiation risk and is derived primarily from studies of Japanese atomic bomb survivors.⁹⁷

Measurement or calculation of effective dose is generally very difficult because the determination of the radiation dose to the body organs is very difficult, and direct measurement is not possible. So, effective dose from a particular imaging procedure is obtained by multiplying measurable dosimetric quantities by a Monte Carlo derived semi empirical conversion coefficient, k. Measurable dosimetric quantities include air kerma, ESE, dose area product (DAP) of entrance skin dose, absorbed dose, CTDI_{air} or DLP. For example:

$$E \text{ (mSv)} = \text{DAP}[\text{mGy cm}^2] \times k \left[\frac{\text{mSv}}{\text{mGy cm}^2} \right] \quad (2.24)$$

in radiographic planar imaging⁹⁸ and

$$E(\text{mSv}) = \text{DLP}[\text{mGy – cm}] \times k \left[\frac{\text{mSv}}{\text{mGy – cm}} \right] \quad (2.25)$$

in CT imaging.^{99,100} The conversion coefficients have been calculated for most imaging modalities.

A traditional dosimetric quantity called ESE is proportional to absorbed dose and hence the effective dose. Since it is easy to measure, it is frequently used in comparing techniques for various radiologic procedures. It is a measure of exposure in units of Roentgen (R) or milli Roentgen (mR) at the skin surface where radiation enters the body.^{101,102} We are going to use ESE in assessing the dose reduction capability of IPS.

Though the thermo luminescence dosimeter (TLD) placed on the skin of the patient can directly measure the ESE,^{103,104} it is not in common use as it requires a lengthy time for annealing and reading process. Another indirect method of determining the ESE consists of measurements of DAP using a large area transmission full-field ionization chamber placed in the beam between the final collimators of the x-ray tube system and the patient.^{105,106} But it then requires a conversion factor to determine the entrance skin dose or exposure. Measurement of DAP is not feasible in our clinic with the Varian OBI imager system.

2.5 Mutual Information

In image analysis, mutual information (MI) serves as an image similarity metric to evaluate quantitatively the similarity between two images. The concept of MI comes from information theory.^{107,108} The MI (A,B), between two images A and B, can be determined from the entropy of the individual images H (A) and H (B) and their joint entropy H (A,B).¹⁰⁹

$$M.I.(A, B) = H(A) + H(B) - H(A, B) \quad (2.26)$$

Thus, the MI index represents how much uncertainty about one image is reduced by the knowledge of the second image. It can be considered as a measure of how well one image explains a second image.¹⁰⁸ If A and B are independent, then A contains no information about B and their MI is therefore zero. If A and B are identical, their MI is maximized. MI measurements consider the intensity distribution of both image data sets. All three terms in equation (2.26) rely only on the probability of occurrence of the various intensities, independent of their spatial distribution.¹¹⁰

The information available in an image can be measured by its entropy. The entropy represents the amount of uncertainty, surprise or information gained from a measurement that specifies one particular value.¹¹¹ Suppose image A is represented by a set of intensity values a_1, a_2, \dots, a_n and B is represented by a set of intensity values b_1, b_2, \dots, b_n . Let $p(a_1), p(a_2), \dots, p(a_n)$ be the probabilities for measurements performed on A yielding the intensities a_1, a_2, \dots, a_n . Similarly, let $p(b_1), p(b_2), \dots, p(b_n)$ be the probabilities for

measurements performed on B yielding the intensities b_1, b_2, \dots, b_n . The Shannon-Wiener entropy measure H is the most commonly used measure of information in signal and image processing. It involves only the distribution of probabilities. Then entropies of A and B are given by:^{109,112}

$$H(A) = -\sum_{i=1}^n p(a_i) \times \log_2(p(a_i)) \quad (2.27)$$

$$H(B) = -\sum_{i=1}^n p(b_i) \times \log_2(p(b_i)) \quad (2.28)$$

Entropy of the image is calculated from the image intensity histogram in which the probabilities are the histogram entries.¹⁰⁸ An image consisting of almost a single intensity will have low entropy, whereas the image with roughly equal quantities of different gray scales will have high entropy.

The joint entropy $H(A, B)$ can be calculated using the joint histogram of two images. Each point and its associated intensity in one image will correspond to a point and its respective intensity in the other. Joint intensity histogram is a two-dimensional scatter plot of image intensity of one image against the corresponding image intensity of the other. A joint intensity histogram can be constructed for a pair of images to estimate the probability of occurrence of each intensity pair together at corresponding locations in the two images. The joint entropy is defined as:^{113,109,114}

$$H(A, B) = - \sum_{i=1}^n p(a_i, b_i) \times \log_2(p(a_i, b_i)) \quad (2.29)$$

where $p(a_i, b_i)$ is the joint probability which represents probability of co-occurrence of a_i , and b_i . Therefore, joint entropy measures the amount of information we have in the two images combined.^{111,113,115}

CHAPTER 3: FEASIBILITY OF AN IMAGE PLANNING SYSTEM FOR IMAGE-GUIDED RADIATION THERAPY

3.1 Introduction

Image guidance has become the standard of care for many treatment scenarios in RT. This is most typically accomplished by use of kV x-ray devices mounted onto the Linac gantry that yield planar, fluoroscopic, and CBCT images. However, image acquisition parameters are chosen via preset techniques that rely on broad categorizations in patient anatomy and imaging goal.

In current practice, the addition of imaging and therapy doses in a meaningful way is suspect. Our project will allow for the addition of these doses, and therefore enable the clinical and scientific evaluation of the associated radiation risks. Dynamic target tracking requires that imaging be performed in real time, and extend for the duration of the radiation delivery. This scenario would benefit from the ability to prospectively calculate and optimize imaging dose. Further, the routine practice of RT planning involves the simulation of radiation beam geometry, and the calculation and review of spatially and dosimetrically accurate doses. The evolution of this practice into imaging dose is technologically and procedurally feasible.

One may consider that the dependence of image quality on patient dose behaves in a manner that is illustrated in Figure 3.1. The image quality, for example contrast-to-noise ratio (CNR), increases with increasing patient dose up

to a point. Above the point of object detectability, additional patient dose does not result in significant or useful improvements in image quality. And for even higher doses, the detector reaches saturation and image quality degrades. Also illustrated is an indication of the minimum image quality required to detect a feature of interest. The optimal imaging technique results in detectability of the features of interest while exposing the patient to minimum dose. Figure 3.1 also

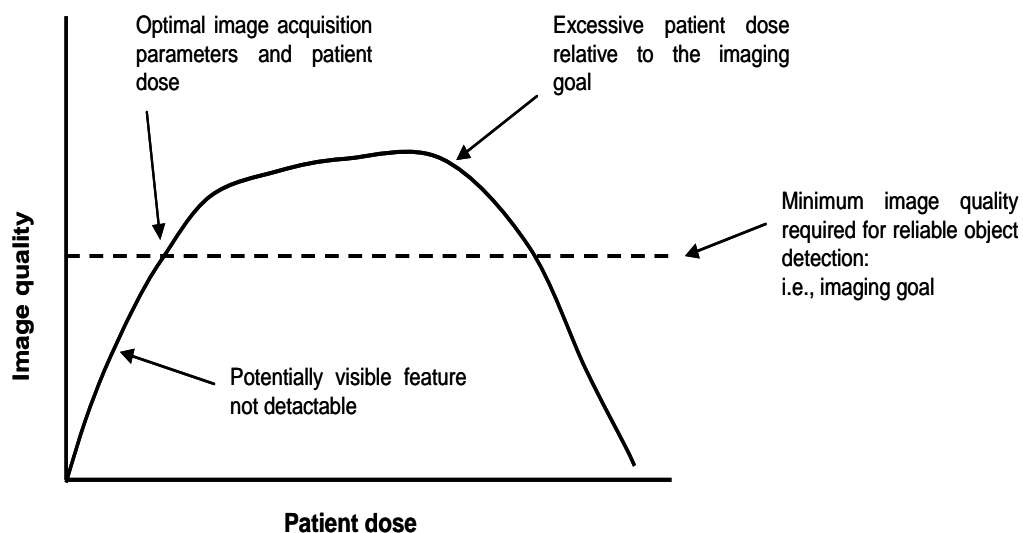


Figure 3.1: The quality of an image is a function of the imaging dose received by the patient. The dotted line indicates the minimum image quality required to detect a given feature of interest. Without overt image planning, it is probable that most clinical images are acquired using suboptimal techniques. Insufficient exposure can leave potentially detectable features masked by image noise, while excessive exposure yields unnecessary patient dose.

illustrates a line below which the image quality is insufficient to detect a potentially visible feature. The region above this line represents an opportunity

that exists in RT localization, in that it may be considered acceptable to increase the imaging dose substantially in order to detect certain anatomic features.

The goals and constraints that are relevant in a radiotherapy context differ from those in a diagnostic imaging context. Specifically, the availability of the planning CT scan provides accurate measures of patient size, anatomical detail and tissue densities. The goal of imaging is to reveal the geometric location of the target tissue or local surrogates. Because our patient population suffers from cancer and the accurate localization of target tissues has the potential to improve outcomes, the risk-benefit optimization is different than in diagnostic imaging settings, and often higher imaging doses can be justified. These considerations are summarized in Table 3.1.

Table 3.1: Differences in the use of imaging procedures in the context of radiotherapy are compared to those in diagnostic imaging.

	Radiotherapy		Diagnostic Imaging	
Characteristic	Properties	Image acquisition parameters	Properties	Image acquisition parameters
Regional anatomy and tissue densities	Known via planning CT scan	Can be determined precisely for every patient	Estimated from patient size and physical exam	Estimated, modified via iteration and automatic exposure controls
Imaging goal	To visualize the geometric extent of known disease or local surrogates	Field of view and required contrast are known	Determine abnormal pathology or lack thereof	Wide field of view and large dynamic range required
Dose constraints	Wide latitude based on patient population and potential ease or difficulty of visualizing imaging goal	Larger doses can be justified if required	Imperative to reduce dose	Tradeoffs between dose and image quality are generalized based on population statistics

Herein, we present an investigation into the feasibility of developing an IPS for radiotherapy. In this first phase, we focus on developing an algorithm that can predict the absolute values of tissue contrast that will be produced by a common radiotherapy planar imaging chain. Input parameters include the CT

data set of the object of interest, as well as simulated planar imaging technique settings that include kV and mAs. The response of the FPD is characterized and integrated into the image simulation algorithm.

We chose to focus initially on simple planar imaging as a feasible first step, and anticipate that further development will enable optimization in fluoroscopic and CBCT applications. Planar kV imaging is widely used to affect three-dimensional patient alignment through the acquisition of an orthogonal pair immediately prior to treatment. The daily kV planar images are compared to DRRs that are produced by the treatment planning system or CT simulator software.

DRRs are constructed by performing a divergent ray trace through the CT data set, with the source of the trace coincident with the x-ray source and the image plane coincident with a defined plane, typically either the plane of isocenter or the imaging detector. Attenuation through the patient or object of interest is calculated for each ray trace and the resulting transmitted intensity is mapped to a grey scale value. Voxel-specific attenuation can be calculated knowing the CT-derived attenuation coefficient and a CT-to-electron density conversion table that is experimentally measured. The image simulation algorithm that we are developing is similar to a basic DRR reconstruction, but differs in several key aspects. Specifically, it is designed to simulate the response of the imaging receptor, and incorporates the beam quality and intensity as input.

Existing commercial DRR algorithms have user-selectable reconstruction options such as soft tissue or boney anatomy windows, and depth-of-field selection^{116–118} However, the purpose of the DRR is to provide a benchmark against which daily planar images can be compared. The powerful, but arbitrary reconstruction tools associated with commercial DRR algorithms do not assist in the prediction of the characteristics of the daily set-up images, and therefore may reveal or mask image detail in a different manner than is present in the daily set up images. Because the goal of daily imaging is to yield consistent and reproducible patient alignment, it is logical to endeavor for accurate image prediction rather than reconstruction of imaging detail a goal which would not exist in the daily set up images. We also note that not all imaging goals are achievable, especially using simple planar imaging techniques. Our image prediction system will aid in determining which goals are achievable (e.g., boney structure or soft tissue contrast for lung nodules) versus those that are unachievable (e.g., soft tissue contrast in the abdomen or pelvis).

The motivation for this work acknowledges the long experience with radiological technique charts and automated exposure control (AEC) systems.¹¹⁹ These techniques are valuable tools with which reasonable acquisition settings and exposure levels at the detector can be assured. However, they rely on broad generalizations in patient size and tissue densities. AEC systems result in consistent image panel exposure, but are not able to modify the prescribed exposure level when the patient-specific imaging goal warrants increases or

reductions in exposure, or to selectively optimize based on a specific area of interest. Low exposure prescans are used in digital mammography to inform the exposure optimization procedure.^{120–122} This is similar to the approach we describe herein, except that the simulation CT scan acts as the prescan, providing prior knowledge of the subject contrast.

Radiation transport in patient anatomy and imaging detector panels is most accurately modeled using Monte Carlo methods. These techniques have most commonly been used to calculate patient dose, most often in CT applications.^{123–127} In addition, the response of FPDs has been studied using Monte Carlo techniques.^{128–130} While these techniques could be applied to our application, they are cumbersome to use and require excessive computation time that undermines their practicality in a clinical setting. As such, we developed an analytical algorithm to calculate the predicted image parameters.

3.2 Methods and Materials

The algorithm, written in Matlab (The Mathworks, Natick, MA), performs a divergent ray-trace through a 3D CT data set and impinges on a flat imaging receptor. Energy-specific attenuation through each voxel of the CT data set is calculated to derive a net transmitted intensity. In this process, the CT number for a given voxel is converted to electron density, and the energy-specific attenuation coefficient for water is found via a lookup table. In this feasibility

study, the variation in atomic number is not overtly taken into account. We justify this simplification based on the fact that Compton processes dominate the interactions at the energies of interest (i.e., 70-150 kVp) and that atomic number information is not presently attainable in the CT simulator used in this study nor in most commercial systems of which we are aware. The detector response as a function of beam quality and exposure was measured and integrated into the algorithm. It is primarily this latter feature that distinguishes the IPS from a traditional DRR.

We conducted experiments designed to quantitatively assess the predictive accuracy of the planning algorithm. These primarily included assessments of soft tissue contrast resolution in phantoms. Specifically, the contrast and geometric appearance of a tissue-equivalent lung nodule embedded in a lung phantom was compared between the IPS and measurements. Small differences in soft tissue contrast were verified using a mammography step wedge QA device. Contrast between boney anatomy and soft tissue was verified using two multimodality imaging phantoms.

A Quasar Programmable Respiratory Motion Phantom (Modus Medical Systems, London, Canada) was used to determine object contrast and detectability of a lung nodule test object. Figure 3.2 shows the experimental arrangement used to acquire the measured data. Projections of the OBI images of the phantom were acquired at different technique parameters. Comparisons between simulated and measured images were made in terms of subject contrast

and dimension of a lung nodule in these images. For all experiments, a GE Lightspeed CT simulator was used to acquire the CT datasets used for the image simulation algorithm.



Figure 3.2: Experimental setup. Respiratory phantom was placed on the Linac couch and AP projection images were acquired at 80 mAs over a wide range of exposure.

The mammography step wedge phantom, Model 081 (CIRS Tissue Simulation and Phantom Technology, Norfolk, VA) was placed on top of water equivalent slabs that were 19 cm in total thickness. Figure 3.3 shows the experimental arrangement used to acquire the measured data of the phantom. The variation in pixel intensity across the step wedge was measured in the simulated and measured images of the phantom at 80 and 120 kVp.



Figure 3.3: Experimental setup. Mammography phantom was placed on top of 19 cm of acrylic slab to get the appreciable level of attenuation along different wedges of the phantom. AP projection images were acquired at 80 and 120 mAs over a wide range of exposure.

Two abdominal phantoms, the Triple Modality 3D Abdominal Phantom, Model 057 and the Image-Guided Abdominal Biopsy Phantom, Model 071 (both from CIRS Tissue Simulation and Phantom Technology, Norfolk, VA), were also studied to assess the contrast between the vertebral bodies and the adjacent soft tissue. The composition of these phantoms is designed to mimic x-ray properties for kV imaging. The boney structures are composed of a calcium-doped epoxy and have an effective atomic number of 8.9. Figures 3.4 and 3.5 show the relevant experimental arrangements using these phantoms.

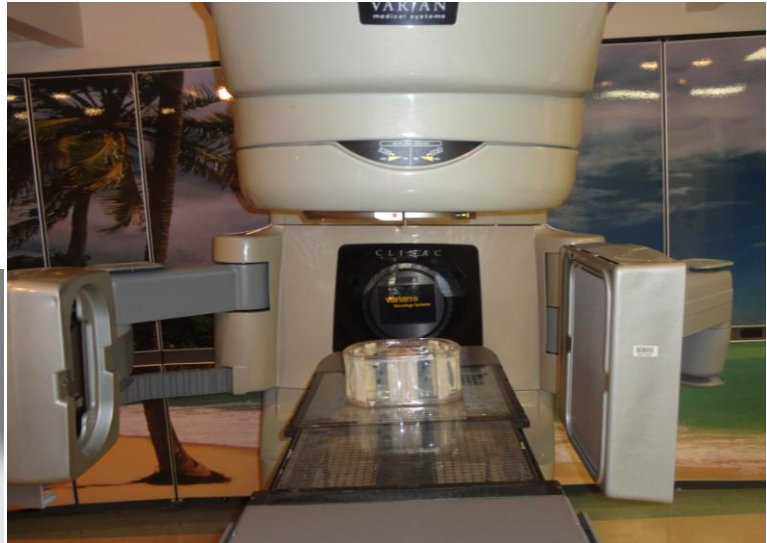


Figure 3.4: Experimental setup. Abdomen phantom model 057 was placed on the Linac couch with flat face lying on the couch. AP projection images were acquired at 80 and 120 mAs over a wide range of exposure.



Figure 3.5: Experimental setup. Abdomen phantom model 071 was placed on the Linac couch with flat face lying on the couch. AP projection images were acquired at 80 and 120 mAs over a wide range of exposure.

Measured data were acquired using a Varian 2100 EX Linac (Varian Medical Systems, Palo Alto, CA) equipped with the OBI system. The OBI consists of a kilovoltage x-ray tube and aSi FPD mounted onto the gantry perpendicular to the treatment beam. The imaging system is capable of producing planar and cone-beam-CT images, although we focus here on the properties of the planar imaging system.

The response of the FPD was characterized by measuring the resulting pixel intensity as a function of unattenuated exposure at the detector surface. Exposure measurements were made using a calibrated Unfors XI Base Unit and Unfors XI Probe (RaySafe Xi system, Unfors RaySafe, Inc., Hopkinton, MA). These measurements were repeated over a range of input intensities (i.e., mAs values) and for 80 and 120 kVp beam qualities. The source-to-detector distance was 150 cm. The pixel intensity was measured by importing the images into Matlab and averaging over the 20 cm x 20 cm field of view. The full dynamic range at each kVp setting was characterized, and these data were integrated into the planning algorithm in the form of kVp-specific lookup tables.

Contrast was measured by selecting an 8 x 8 pixel ROI in either the lung nodule or vertebral body and comparing the average intensity to a similar ROI in the adjacent soft tissue. This is described in equation (3.1), where $Intensity_{ROI}$ and $Intensity_{bkg}$ are the pixel intensities measured in the region of interest and background, respectively.

$$\text{Contrast} = \frac{\text{Intensity}_{\text{ROI}} - \text{Intensity}_{\text{bkg}}}{\text{Intensity}_{\text{bkg}}} \quad (3.1)$$

The uncertainty in the measured contrast was estimated using the equation:

$$\text{Error in Contrast} = \frac{\text{Intensity}_{\text{ROI}}}{\text{Intensity}_{\text{bkg}}} \times \left[\left\{ \frac{\sigma(\text{Intensity}_{\text{ROI}})}{\text{Intensity}_{\text{ROI}}} \right\}^2 + \left\{ \frac{\sigma(\text{Intensity}_{\text{bkg}})}{\text{Intensity}_{\text{bkg}}} \right\}^2 \right]^{1/2} \quad (3.2)$$

where $\sigma(\text{Intensity}_{\text{ROI}})$ and $\sigma(\text{Intensity}_{\text{bkg}})$ represent the standard deviation of intensity in the ROI and background respectively.

3.3 Results

The response characteristics of the imaging detector are shown in Figure 3.6. As anticipated, pixel intensity increases linearly with exposure prior to

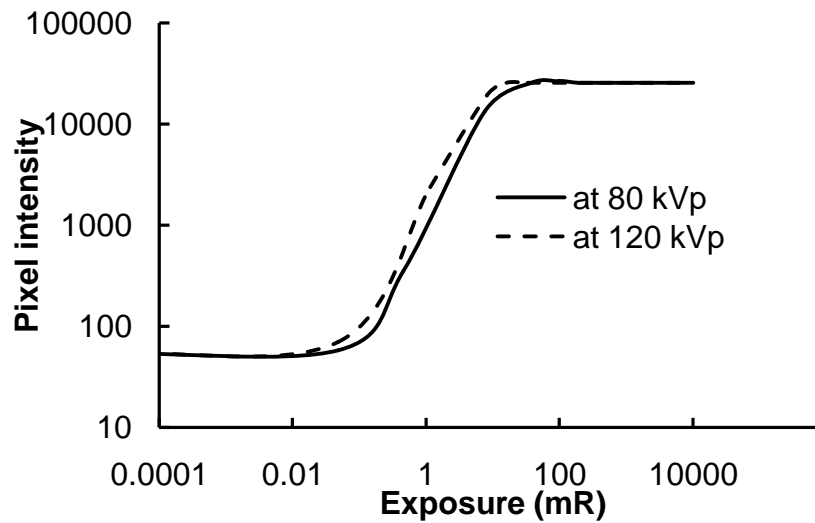


Figure 3.6: The response curve of the imaging detector is shown. These data were integrated into the IPS algorithm to predict absolute values of tissue contrast.

reaching saturation. The energy independence of the detector response is evident in the data. The saturation point of the detector is used in the planning algorithm to predict degradation in object detectability due to over-exposure. Optimal acquisition techniques will result in image features with appreciable contrast at low exposure levels.

We studied a lung nodule test object to assess the planning system's ability to predict object contrast and detectability. Simulated images were constructed over a range of mAs values for 80kV beam quality. The resulting contrast was assessed by plotting absolute pixel intensity values across the region of interest. These data are plotted in Figure 3.7. The simulated data

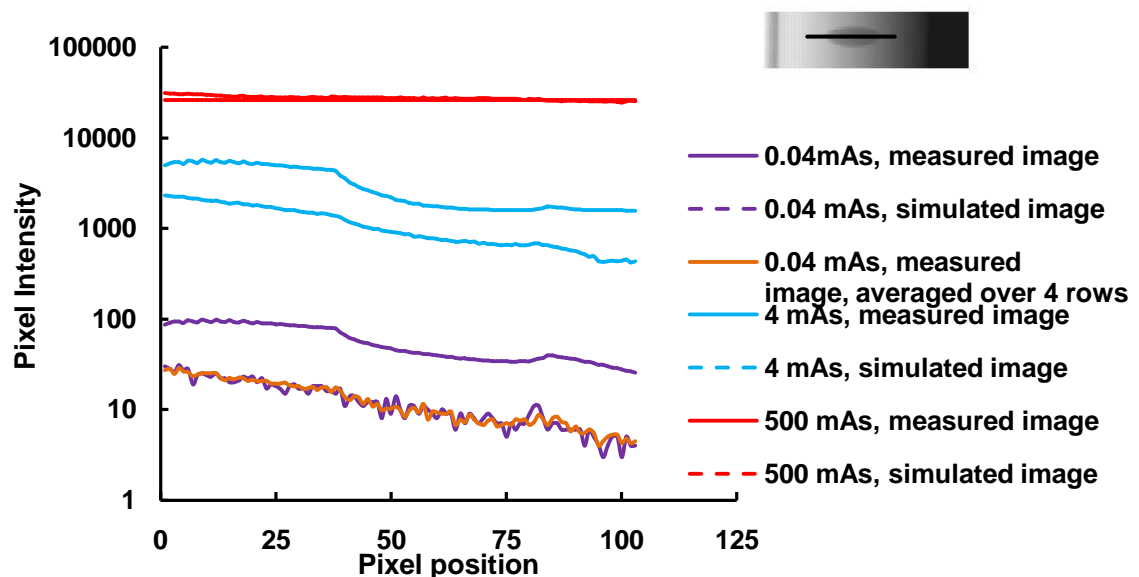


Figure 3.7: The absolute values of the pixel intensity across the lung nodule embedded in lung tissue are shown. The edges of the nodule can be appreciated in both the simulated and measured images. Noise becomes appreciable at low mAs levels and begins to obscure the nodule in the measured image.

agree with measured data in that the slope of pixel intensities appears similar, and the presence of the nodule is evident. Further, image saturation at high mAs values is evident in both images. However, there is a systematic offset between the image pairs, with the absolute value of the pixel intensity being higher in the simulated images. We believe that this may be a limitation of the mono-energetic approximation used in this study, although we note that the resulting nodule visibility is similar in both images. Image noise becomes appreciable at low mAs levels and begins to obscure the nodule in the measured image. This is not evident in the simulated images as we have not yet incorporated a noise model into the algorithm.

The geometric appearance of the spherical lung nodule in the respiratory phantom is a function of the exposure level and image detector saturation. As saturation is approached, the peripheral contrast and spatial dimensions of the nodule vary. To study this, we assessed the vertical dimension of the lung nodule in the measured and simulated images. Good quantitative agreement is seen in Figure 3.8 and affirms the algorithm's predictive capabilities. Representative image pairs are shown in Figure 3.9. The invariance of the contrast with kVp and mAs prior to saturation is predicted, as well as the gradual loss of object detectability and dimension as saturation is approached. The saturation mAs level for the 80 kVp beam is higher than the 120 kVp beam, as would be expected.

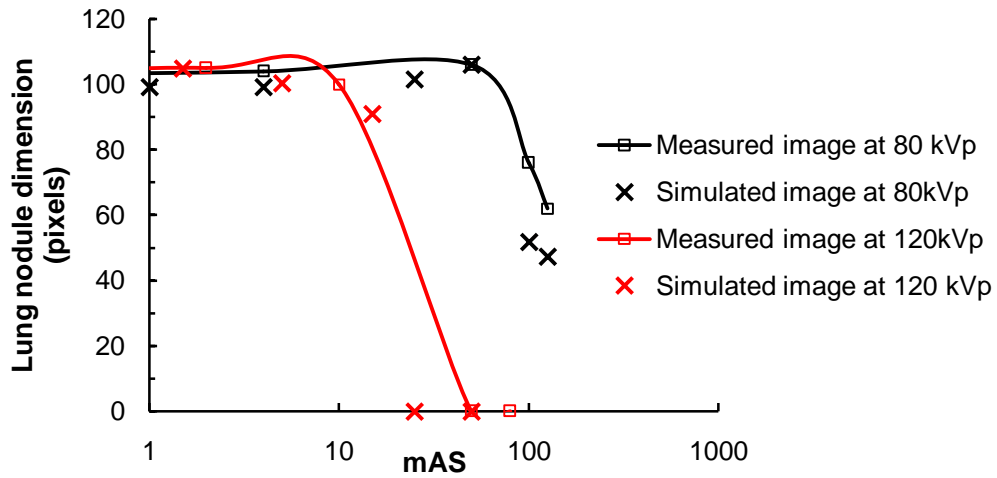


Figure 3.8: The geometric appearance of the lung nodule in the respiratory phantom is a function of the exposure level and image detector saturation. The vertical dimension of the visible nodule is predicted by the IPS. The error bars indicate the uncertainty in the measurement of the diameter of the lung nodule, and are based on the lack of discrete contrast levels at the lung nodule boundary.

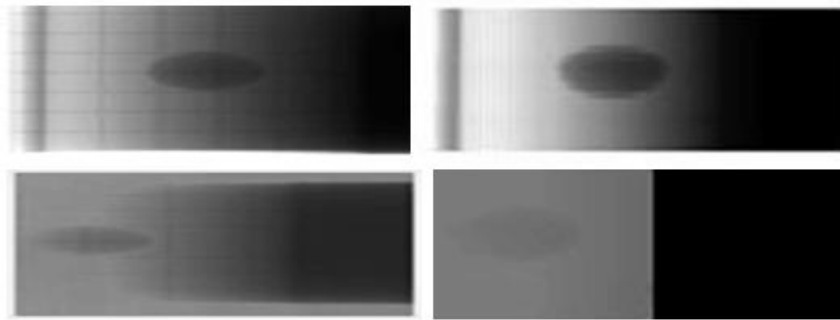


Figure 3.9: As the image approaches saturation at high mAs values, the nodule gradually becomes less visible and its geometric dimensions vary. The top row compares measured (left) and simulated (right) images acquired at 4mAs and 80 kVp. The bottom row compares measured (left) and simulated (right) images acquired at 100 mAs.

The ability of the IPS to predict small changes in soft tissue density was studied using the mammography step wedge phantom placed on top of 19 cm of polystyrene. The variation in pixel intensity over the range of steps is compared between the measured and simulated images in Figure 3.10. Data were acquired at beam qualities of 80 and 120 kVp and over exposure values ranging from 0.04 to 500 mAs. The lower exposure value used was the minimum setting available on the OBI system, while the maximum setting corresponded to image

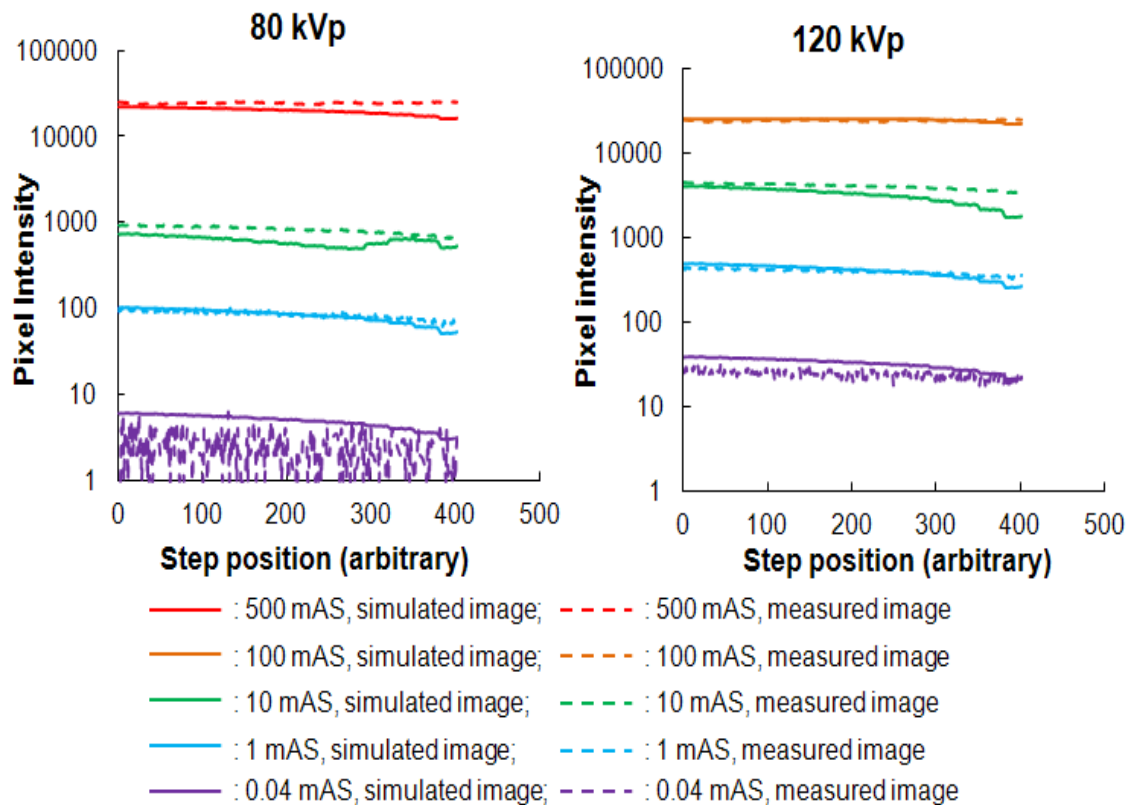


Figure 3.10: The variation in image detector response is plotted across the mammography step wedge. Comparison between simulated and measured images shows good agreement over a wide range of exposure levels and beam qualities.

saturation, i.e., 500 mAs at 80 kVp and 100 mAs at 120 kVp. The data show good agreement in terms of the absolute value of pixel intensities predicted, as well as small variations across the step wedge pattern. The saturation pixel intensity was consistent between the two beam qualities studied. The small but observable slope in the pixel intensity across the step wedge pattern is observed to be similar in the measured and simulated images.

In Figure 3.11 we compare the simulated and measured images of the mammography step wedge phantom. Data were collected for these images at 10 mAs and 80 kVp. Qualitatively, there is good visual agreement between the two images, both in terms of geometric integrity and contrast predictability.

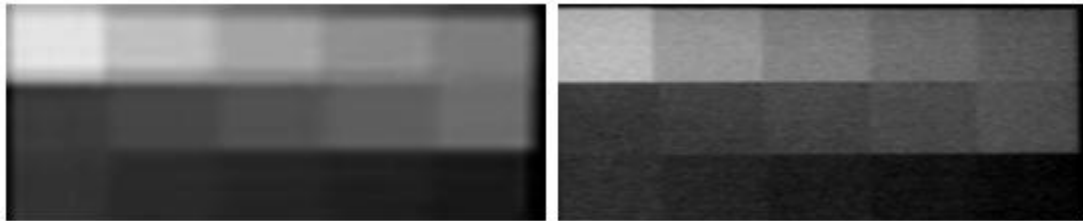


Figure 3.11: The measured image (left) and simulated image (right) of the mammography step wedge phantom is shown. Data were acquired at 10 mAs exposure level and 80 kVp beam quality. There is good geometric and visual agreement between the two images.

Boney tissue contrast was assessed using the two abdominal phantoms and contrast assessment using methods described above. Measured and simulated images were generated over a range of mAs values for 80 and 120 kVp beam qualities. The exposure intensity range was selected to span the

minimum value selectable up through detector saturation. The data are shown in Figure 3.12. Measured and calculated values agree in terms of predicting the mAs value at which detector saturation, and subsequent loss of contrast occurs. There is a systematic offset between the measured and simulated data that may be due to our simplifications in the beam quality. The lack of variation in contrast over mAs values lower than 10 suggests that there is wide latitude for minimizing patient dose.

The data in Figure 3.12 indicate the potential utility of the IPS. It correctly predicted that the difference in contrast between the two beam qualities studied is minimal and likely not clinically significant. IPS predicted the invariant contrast

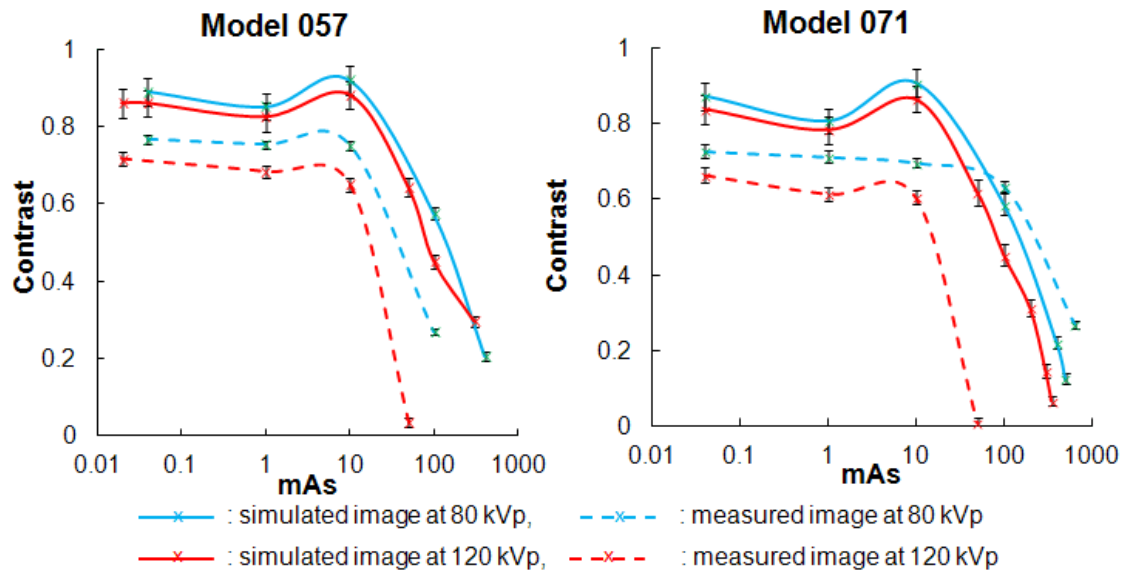


Figure 3.12: The contrast between the vertebral body and surrounding soft tissue is shown for the two abdominal phantom models studied. The image simulation algorithm predicts the input exposure level (i.e., mAs setting) at which image saturation and subsequent loss of contrast occurs.

with increasing mAs setting, prior to saturation. In addition, IPS predicted the mAs setting at which saturation would occur. The images used for this comparison are shown in Figure 3.13.

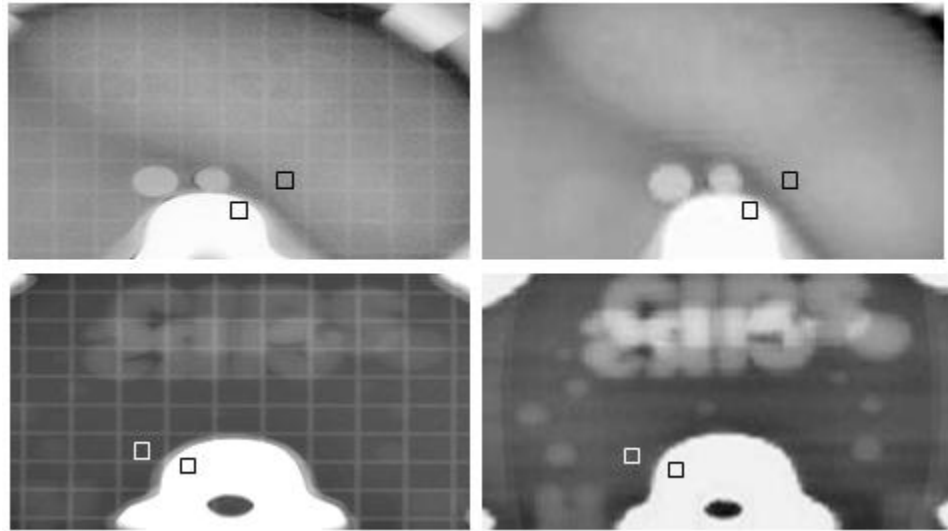


Figure 3.13: Measured (left) and simulated (right) images are compared for two abdominal phantoms. Images presented in the top row are from the 057 phantom and those in the bottom row are from the 071 phantom. Boxes indicate the regions of interest used to assess the contrast.

3.4 Discussion

The data presented herein are promising in that they support the ability of IPS to predict the following image characteristics.

- Absolute values of pixel intensities and image contrast
- Invariance of image contrast with beam quality (over the range studied)

- Loss of object visibility as saturation or underexposure is approached

This information will enable the planning of image acquisition techniques that reduce patient dose while maintaining the contrast required to achieve the imaging goal. This process is illustrated in Figure 3.14. Soft tissue contrast was modeled using the mammography step wedge phantom placed on top of 19 cm of polystyrene and a 1 mm fiducial BB was located to the right of the phantom. Simulated images are shown in the top row and were derived by using the thorax preset values contained in our clinical system (80 kVp, 10 mAs). Measured images are shown in the bottom row. Possible improvements in soft tissue contrast with changes in kVp were assessed iteratively and an alternate image acquisition technique is included (120 kVp, 5 mAs). Of note is that there is no clinically relevant change in the contrast between the ROIs indicated in the figure between the two kVp settings simulated.

The selection of the imaging goal can then proceed. For example, if a soft tissue target is desired and the contrast appears sufficient to be clinically reliable (e.g., contrast between ROI 1 and ROI 3), then this may be selected as the imaging goal, and the image acquisition parameters can be adjusted to reduce patient dose as low as reasonable while maintaining contrast. If however, the desired soft tissue target has insufficient contrast to be considered clinically reliable, despite optimization of image acquisition parameters (e.g., contrast between ROI 1 and ROI 2), then this goal may be abandoned. In such a case, an implanted fiducial marker would be a viable surrogate and appropriate imaging

goal. The image acquisition parameters would then be optimized to visualize the fiducial marker, and patient dose reduced such that regional anatomy is rendered minimally recognizable.

This is illustrated in the right-most image in Figure 3.14, in which the BB remains clearly visible. Patient entrance exposure for this image is reduced by approximately a factor of 5, compared to the other two images. Experimental validation of this process is contained in the bottom row of Figure 3.14, in which the corresponding images were acquired using our clinical equipment.

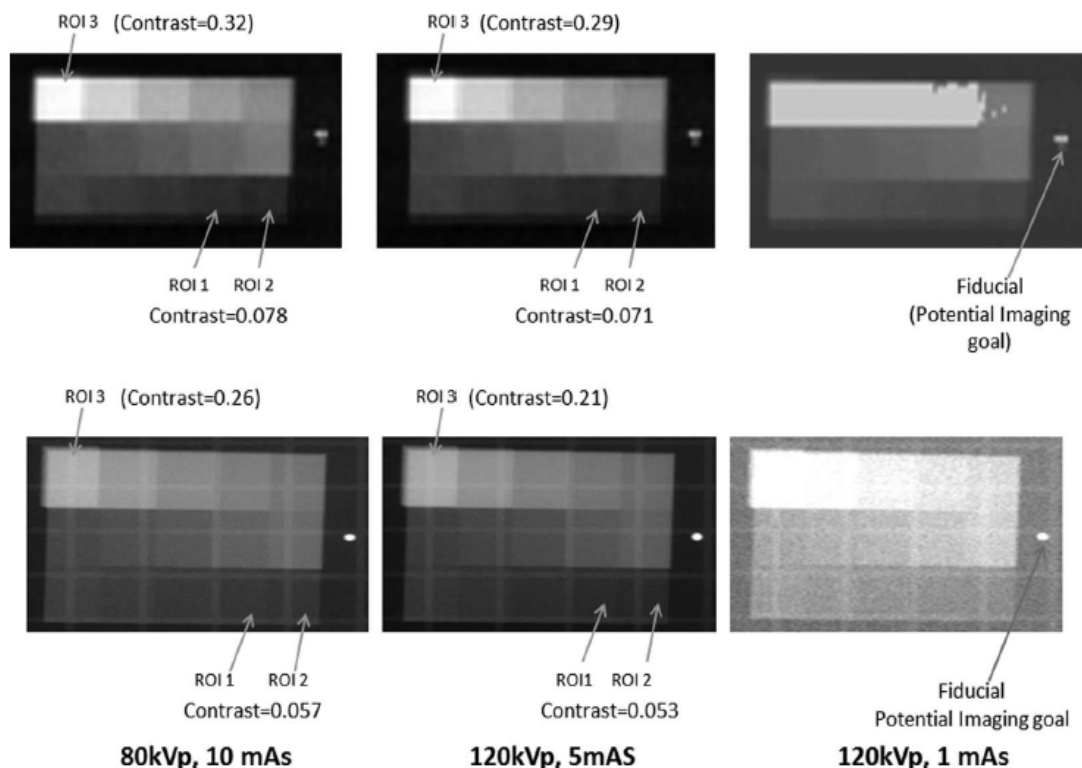


Figure 3.14: An example of the use of the IPS in selecting an imaging goal is shown. Top row: simulated images assessing differences in contrast using different kVp and mAs settings. Bottom row: measured images. Selection of the

imaging goal could include soft tissue differentiation, e.g., ROI 3 which is likely to be reliably visible versus ROI 1 which is not likely to be clinically visible. Reduction in dose is achieved by declaring the fiducial marker to be the imaging goal (right column). The low contrast lines are a tennis racquet on the Linac table.

As a next step, we plan to begin clinical testing and to incorporate a simple entrance exposure calculation into the algorithm to assist in the planning and decision process.^{131–133} Other volumetric dose calculations may be readily integrated into the algorithm, if deemed advantageous.

The simulated image data presented herein were created using a computationally efficient monoenergetic beam approximation. Although this is an oversimplification, we evolved to this method due to its predictive accuracy. As written, the simulation algorithm is capable of modeling a heterogeneous beam spectrum. We modeled the beam spectrum using SpekCalc software,¹³⁴ but this produced results for which the measured and simulated image data did not agree. We speculate that this may be due to inaccuracies in the modeled inherent filtration or other tube characteristics that are difficult to assess definitively due to vendor proprietary concerns.

The monoenergetic approximation yields functionally sufficient agreement between measured and simulated data. Notwithstanding, there appears to be a systematic offset between the simulated and measured images in Figure 3.7 and

Figure 3.12. We expect that inclusion of an accurate beam heterogeneity model, coupled with noise and scatter models, will resolve this offset.

The lower limit on the incident exposure level will be dictated by detector noise and scatter. Although we investigated primitive noise models, we found their benefit to be limited and did not incorporate them at present. This is due to the fact that the minimum exposure setting (i.e., mAs setting) generally yielded images in which the objects of interest were detectable. This is attributable to the relatively small size (20 cm maximum radiological path length) of the phantoms studied, and the small variation in their subject contrast. Clinically, the algorithm will need to properly predict saturation and under-response in the same image. For example, imaging of the thorax and mediastinum in large patients presents large variations in subject contrast. Inclusion of noise and scatter models will be a topic of future studies.

In its present state, the algorithm excludes differences in attenuation based on atomic number. We believe that this is valid within the context of the proposed application of the algorithm. The OBI system is most often used between 80 and 120 kVp. In this energy range, Compton process dominates which is independent of atomic number of the materials. The effective atomic number (Z_{eff}) for muscle and bone are 7.3 and 12.3, respectively. Z_{eff} for the boney structures in the abdominal phantom is 8.9. These differences are relatively small.

Further development will include modeling of the atomic number dependence of the x-ray absorption properties. Extracting this information from the CT data will require incorporation of novel strategies, but may improve the predictive accuracy of the algorithm. This would be especially relevant for lower kVp imaging scenarios in which photoelectric absorption processes begin to dominate and for very high Z materials such as fiducial markers.

Ongoing work is needed prior to routine clinical implementation. The areas that we anticipate will require further development and testing include the following:

- Resolution of the most appropriate handling of beam spectrum and hardening;
- Incorporation of noise and scatter models;
- Management of atomic number dependencies;
- Inclusion of patient dose assessment.

3.5 Conclusions

We developed and tested an algorithm that can be used to assist in kV imaging technique selection during localization for radiotherapy. The algorithm uses patient-specific CT data sets and integrates the imaging detector response to predict absolute values of pixel intensity and image contrast. Phantom testing

demonstrated the algorithm's predictive accuracy for both low and high contrast imaging scenarios. Detector saturation with subsequent loss of imaging detail, both in terms of object size and contrast, were accurately predicted by the algorithm.

CHAPTER 4: PROSPECTIVE IMAGE PLANNING IN RADIATION THERAPY FOR OPTIMIZATION OF IMAGE QUALITY AND REDUCTION OF PATIENT DOSE

4.1 Introduction

When OBI is used in RT for patient alignment, the region-based contrast of the anatomic feature of interest is considered to be the imaging goal.^{135–137} We developed and tested the IPS that can be used to assist in planar kV imaging technique selection during localization for RT (Chapter 3).¹³⁸ The IPS allows a user to vary the image acquisition parameters and manually optimize them to meet the imaging goal at low dose, if possible. Alternatively, the IPS suggests the techniques that provide increased imaging dose but with improved useful image quality. As such, the IPS facilitates selection of the image acquisition parameters using a cost/benefit analysis.

In Chapter 3, phantom testing established the fact that IPS can predict subject contrast for a range of image acquisition parameters. Results from these studies also verified that the IPS can assess the underexposure, saturation and a contrast plateau over a wide range of acquisition parameters. This chapter includes anthropomorphic phantom data and clinical data to further assess these IPS's capabilities over a wide latitude and its potential for facilitating dose reduction.

4.2 Methods and Materials

4.2.1 Image contrast prediction

A female whole-body adult anthropomorphic phantom (model 702-D; CIRS, Norfolk, VA), was used to test the capability of the IPS in predicting image contrast over a range of mAs and kVp settings. Images from the head and neck, thorax and abdomen, and pelvis- were studied separately. The experimental set up used to generate the AP projection pelvic images is shown in Figure 4.1. Measured images were acquired at mAs values ranging from 0.02 to 600 at 80 kVp beam quality for three sites. Simulated images of these three sites of the



Figure 4.1: The experimental setup. The phantom was placed on the Linac couch and measured images were acquired by means of the OBI system attached to the Linac.

phantom were generated over the same range of mAs values at 80 kVp using the IPS. In the case of the pelvis, we also generated simulated and measured images at 120 kVp beam quality over this range (i.e. from 0.02 to 600) of mAs values.

Qualitative and quantitative assessments were made of the IPS's capabilities in terms of predicting image contrast, underexposure, saturation and the image quality plateau. Qualitatively, visual inspection of the image contrast was compared between measured and simulated images, noting loss of contrast due to imaging panel saturation or under-exposure. We used MI as a quantitative similarity metric^{108,113} to compare measured and simulated images. The reference image was taken to be the measured image acquired at the lowest possible mAs value that achieved sufficient contrast necessary for patient alignment. For example, in case of the pelvic images at 80 kVp, we used the measured image at 5 mAs as the reference. Table 4.1 lists the acquisition values for the reference images used in this study. Subsequent images, either measured or simulated, were produced at different incident exposure (i.e., mAs) values and compared to the reference image.

Table 4.1: Image acquisition parameters for reference image of head/neck, thorax/abdomen and pelvis sites of the anthropomorphic phantom

Site	Reference image acquisition parameters
Head/ Neck	80 kVp, 3 mAs
Thorax/ Abdomen	80 kVp, 3.20 mAs
Pelvis	80 kVp, 5 mAs
Pelvis	120 kVp, 0.5 mAs

For a given beam quality, the MI indices between the reference image and each of the simulated or measured images were calculated separately for each site. Figure 4.2 illustrates this process for the pelvic region of the anthropomorphic phantom with data taken at 80 kVp. The range of simulated or measured images were compared to the reference image. We expect that if the IPS accurately predicts the image appearance, that the MI index will be similar at a given mAs setting for both simulated and measured images, and that the variation in MI over the tested range will behave similarly.

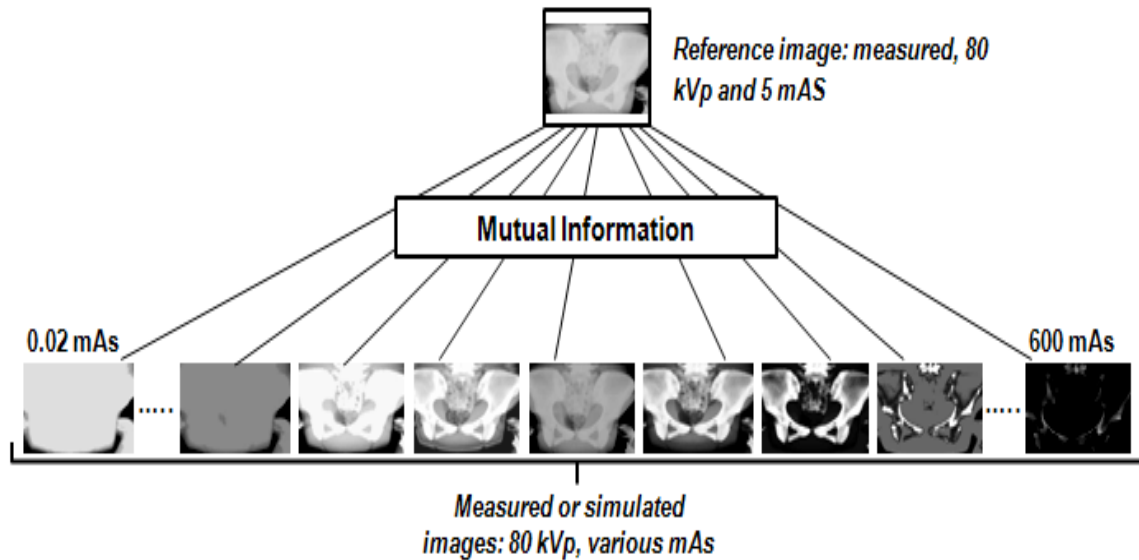


Figure 4.2: At 80 kVp beam quality, simulated images were generated over a range of mAs values and measured image acquired at 5 mAs was taken as the reference image.

4.2.2 Assessment of dose reduction

We used the image planning algorithm to confirm its use as a tool to affect imaging dose reduction without loss of useful image contrast. The IPS was used to suggest acquisition settings for six patients, three of which were treated for disease in the head and neck, and three for disease in abdominal sites.

Consistent with current clinical practice, we considered the imaging goal for these patients to be regional bony anatomy.^{139,140} Specifically, the cervical vertebra for the head and neck patients and the thoracic and lumbar vertebra for abdominal patients were taken as the imaging goal. During image acquisition for

patient alignment, the vendor-preset values for mAs and kVp were replaced with values determined through simulations using the IPS. The therapists in our clinic were asked to assess whether the resulting images were of a similar and useful quality to the images they typically acquire.

Again, we used the MI index to evaluate the similarity between acquired images. For all six patients, the reference image was taken to be the image acquired on the first day of treatment using the manufacturer preset values for mAs and kVp. For a given patient, the MI index between the reference image and each of the images acquired on successive treatment days using the same presets was calculated separately for both AP and lateral projections. This was done in order to quantify the variability in image contrast using our normal clinical procedures. This process is illustrated in Figure 4.3.

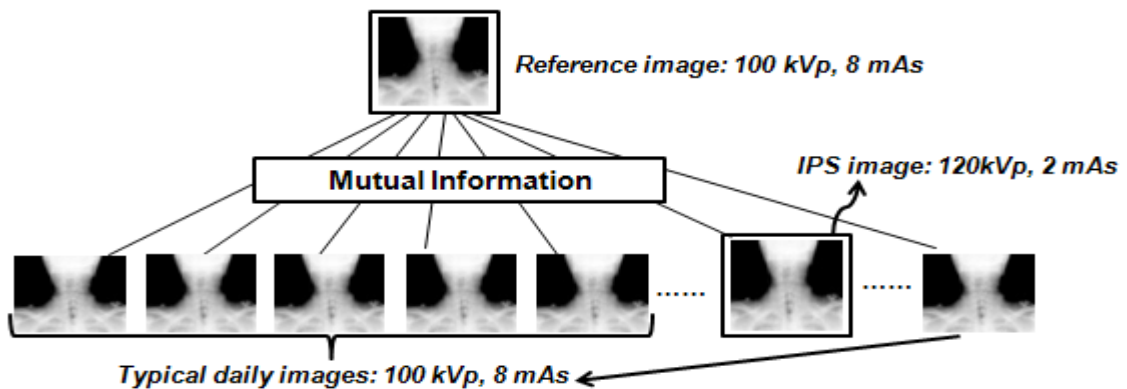


Figure 4.3: The measured images acquired daily using the preset technique factors were used to establish normal clinical variability in image quality. A single, reduced dose image was acquired using technique factors manually derived using the IPS. The clinical image acquired on the first day of treatment was taken as reference image for calculation of the MI index.

Subsequently, we varied the acquisition parameters on one day of treatment to those suggested using the IPS. The revised parameters were selected manually to yield similar contrast to the manufacturer preset values, but to reduce ESE if possible.

ESE was used as a measure of imaging dose. To assess the ESE, we determined the x-ray tube output. For this, a calibrated Unfors XI Base Unit and Unfors XI Probe (RaySafe Xi System, Unfors RaySafe, Inc., Hopkinton, MA) meter was placed on top of the kVD of the OBI system. In our clinic, the separation between the kVS and kVD is held constant at 150 cm. Exposure readings were measured as a function of mAs over a range of kVp values. Figure 4.4 shows the x-ray tube output at 150 cm from the focal spot. The data

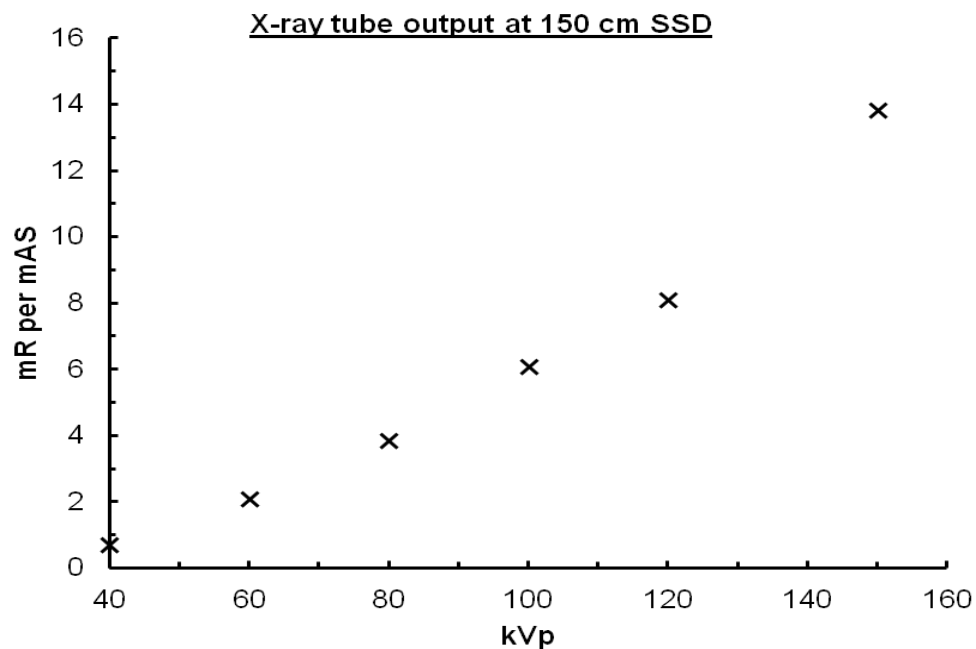


Figure 4.4: Varian x-ray tube output measured at 150 cm SSD is shown.

are consistent with the typical behavior of x-ray tubes in that the output is proportional to the square of the kVp. Experimental confirmation was deemed desirable because this data is used for both ESE calculations as well as calculation of the pixel intensity in the simulation algorithm.

Source to surface distance (SSD) and image acquisition parameters specific to the patient were used to determine the patient specific ESE, given by equation 4.1: ^{141,142}

$$\text{ESE(mR)} = \left[\text{output} \left(\frac{\text{mR}}{\text{mAs}} \right) \right] \times \xi (\text{mAs}) \times \left[\frac{150}{\text{SSD (cm)}} \right]^2 \quad (4.1)$$

Here, output (mR/mAs) represents the exposure per mAs of the x-ray tube for a given kVp value and ξ is the mAs value used in image acquisition.

4.3 Results

4.3.1 Image contrast prediction

In Figure 4.5, we present images of the pelvis site of the anthropomorphic phantom to illustrate the IPS's capability regarding predicting image contrast. The second and third columns compare measured and simulated images at 5 and 10 mAs values at 80 kVp. We see that for both 5 and 10 mAs, corresponding image pairs have similar levels of contrast. Of note is the observation that the images at 5 mAs have sufficient contrast to meet the imaging goal of boney structure

visualization. Thus, the IPS not only predicts image contrast, but also predicts the potential for reducing imaging dose. The left column in Figure 4.5 shows images acquired at the lower limit of available exposure level (i.e. at 0.1 mAs). Note the loss of contrast due to under exposure. Similarly, the right column in Figure 4.5 shows the loss of image contrast due to detector saturation.

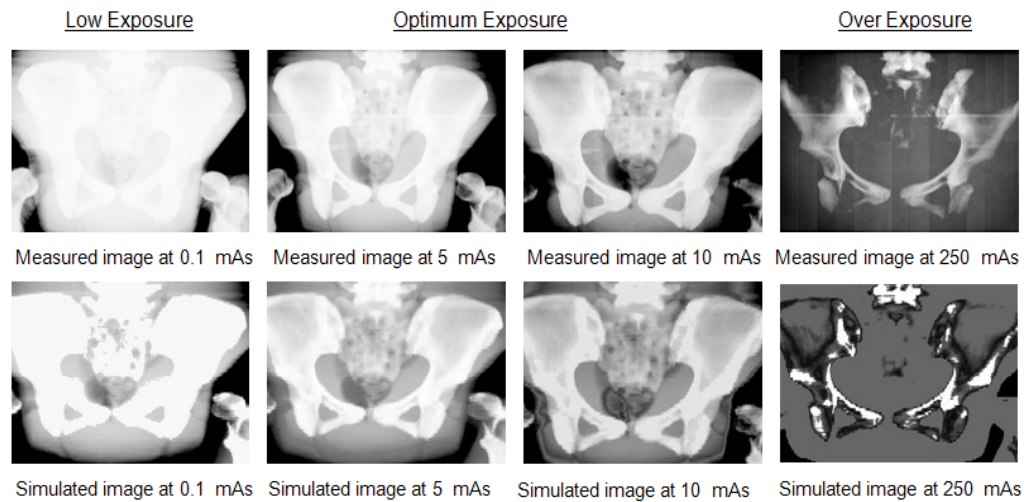


Figure 4.5: Pelvic images of anthropomorphic phantom at 80 kVp. These images illustrate the predictive capabilities of the IPS for subject contrast, under and over exposure and an image quality plateau for a range of image acquisition parameters. Images at 5 and 10 mAs values demonstrate the potential for imaging dose reduction.

In Figure 4.6 we display the behavior of the MI index to assess the similarity between image pairs over a range of exposure levels using the pelvic phantom site. The agreement between the data for measured and simulated

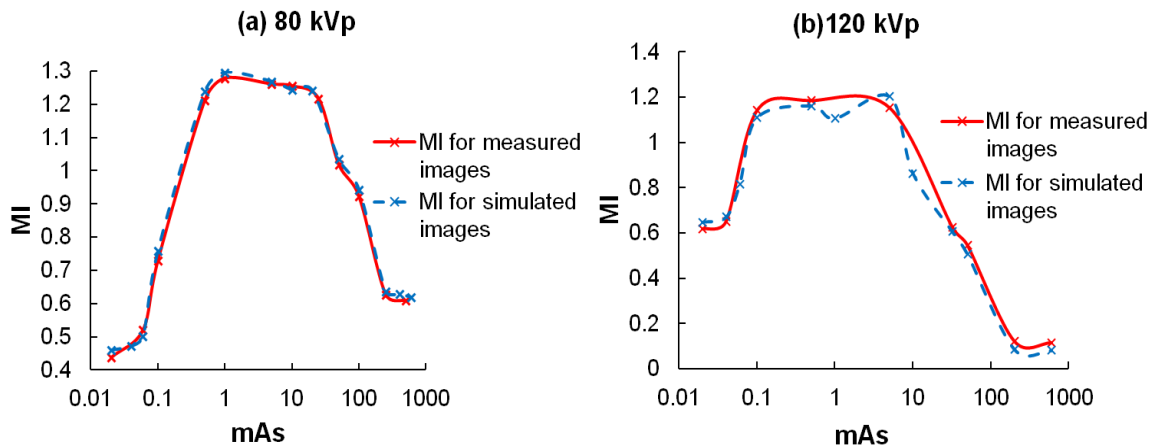


Figure 4.6: Variation of MI for pelvic images of the anthropomorphic phantom at (a) 80 kVp and (b) 120 kVp beam qualities as a function of mAs demonstrates the IPS's predictive capability regarding subject contrast, under and over exposure and an image quality plateau for a range of image acquisition parameters. Note that measured images at 5 mAs and 0.5 mAs were taken as the reference images at 80 and 120 kVp respectively.

image pairs is evident, and supports the assertion that IPS is capable of accurate image contrast prediction. Further, image contrast degrades at both high and low limits of exposure and remains relatively constant over a two-decade range of exposure. This image contrast plateau suggests there is potential clinical utility of the IPS in reducing patient dose without appreciable loss of image contrast.

Figures 4.7 (a) and 4.7 (b) compare simulated images produced using the IPS over a range of mAs settings to the reference image for two additional anatomic sites. Data were produced at 80 kVp beam quality for head/neck and thorax/abdomen sites of the phantom. These data also show that image contrast

degrades at both high and low limits of exposure. The image contrast plateaus for these sites are narrow compared to the pelvis site, although there still appears to be opportunity for patient dose reduction.

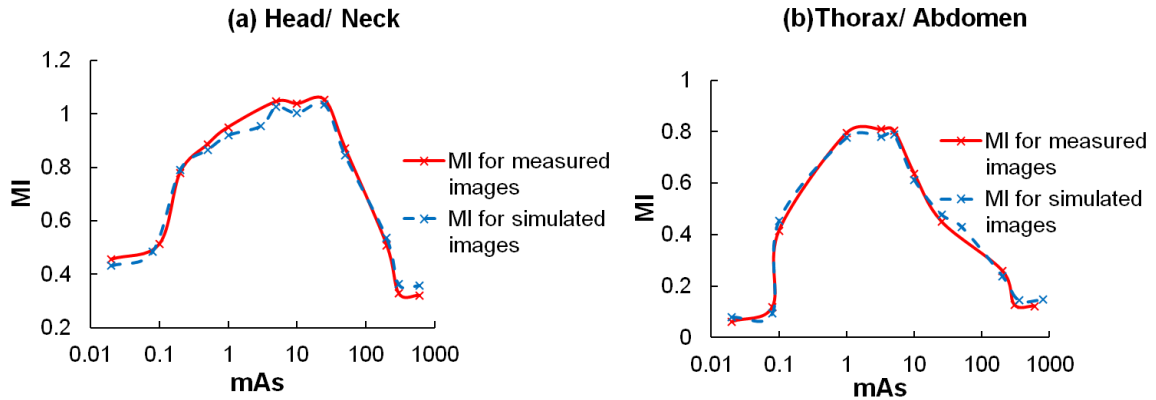


Figure 4.7: Variation of MI as a function of exposure for (a) head/neck site and (b) thorax/abdomen site of the phantom at 80 kVp beam quality. The contrast behavior displayed is consistent with similar data collected for the pelvic region. Note that measured images at 3 mAs and 3.20 mAs were taken as the reference images for the head/neck and thorax/abdomen sites, respectively.

Data collected using the pelvic region of the phantom are shown in Figure 4.8. It illustrates an important result, in that there is no appreciable improvement in image contrast resulting from a decrease in the beam quality. That is, the maximum value of the MI index, or similarity to the optimal contrast image, is not appreciably different for images acquired at 80 and 120 kVp. Note however that the data show that the saturation of the 120 kVp images starts at lower mAs

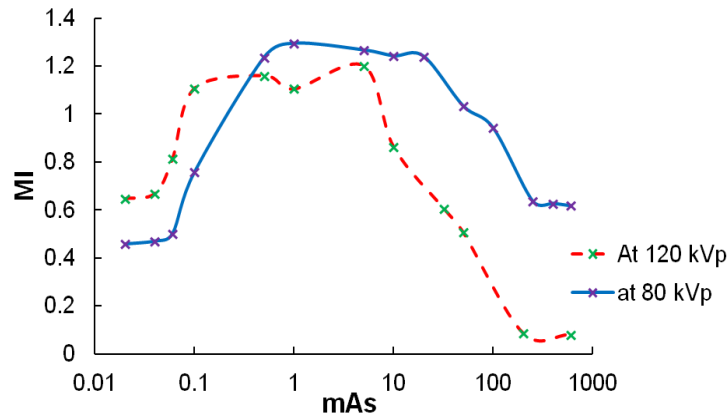


Figure 4.8: Comparison of the MI index between a measured reference image and a range of simulated images is shown. The pelvic region of the anthropomorphic phantom provides the subject contrast and data were generated at 80 and 120 kVp beam qualities. There is no appreciable increase in image contrast at 80 kVp over 120 kVp. The IPS predicts the potential for reducing imaging dose by selecting a high kVp without loss of useful image contrast. Note that measured images at 5 mAs and 0.5 mAs were taken as the reference images at 80 and 120 kVp respectively.

settings, as would be expected. These data suggest that the clinical practice of reducing the kVp in order to improve image contrast should be challenged, at least in the context of radiotherapy alignment, since use of higher kVp settings reduces patient imaging dose.

4.3.2 Assessment of dose reduction

The results of our study to verify the potential for imaging dose reduction are shown in Table 4.2. In all cases studied, we were able to affect a 37% or

greater reduction in imaging dose to the patient compared to the vendor-provided preset acquisition parameters.

Table 4.2: Clinical data demonstrates facilitation of imaging dose reduction.

Patient	Site/projection	Image acquisition parameters		Entrance skin exposure (mR)	
		Preset	IPS revised	Preset	IPS revised
1	Head/Neck, AP	100 kVp, 8 mAS	120 kVp, 2 mAS	94.67	34.73
	Head/Neck, Lat	70 kVp, 5 mAS	80 kVp, 1 mAS	29.02	7.68
2	Head/Neck, AP	100 kVp, 8 mAS	100 kVp, 5 mAS	103.17	64.48
	Head/Neck, Lat	70 kVp, 5 mAS	70 kVp, 1 mAS	30.22	6.04
3	Head/Neck, AP	100 kVp, 8 mAS	120 kVp, 3mAS	98.44	44.94
	Head/Neck, Lat	70 kVp, 5 mAS	80 kVp, 2 mAS	29.45	15.61
4	Abdomen, AP	80 kVp, 32 mAS	80 kVp, 20 mAS	273	170.62
	Abdomen, Lat	85 kVp, 40 mAS	85 kVp, 25 mAS	399.19	199.6
5	Abdomen, AP	80 kVp, 32 mAS	100 kVp, 10 mAS	270	135.02
	Abdomen, Lat	85 kVp, 40 mAS	100 kVp, 15 mAS	424.66	224.28
6	Abdomen, AP	80 kVp, 32 mAS	85 kVp, 25 mAS	266.45	196.41
	Abdomen, Lat	85 kVp, 40 mAS	85 kVp, 25 mAS	409.28	144.11

We verified both qualitatively and quantitatively that this reduction in dose occurs with no loss of image contrast. Therapists were asked to evaluate the contrast of the revised images immediately following acquisition. They found no significant difference between images acquired with the reduced-dose

parameters and typical images acquired using the vendor presets. Subsequently, we calculated the MI index as an image similarity metric. Figures 4.9 and 4.10 compare the MI numbers for the images acquired using the reduced-dose settings to the typical daily images for patient 1 (head/neck site) and patient 4 (i.e. abdominal site) respectively. The data indicate that the contrast produced using optimized imaging protocols is comparable to those typical daily images with preset imaging protocols.

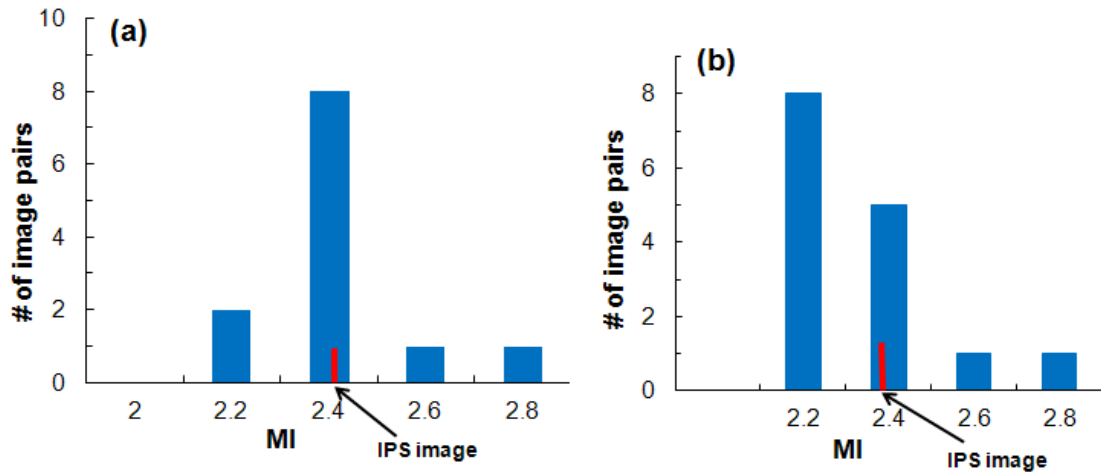


Figure 4.9: The MI index for (a) AP and (b) lateral projections of patient 1(Head/ Neck site) are shown. Histogram data correspond to the range of daily clinical images acquired using standard preset acquisition parameters. The MI values for the reduced-dose images are indicated by the red bars and were predicted by the IPS.

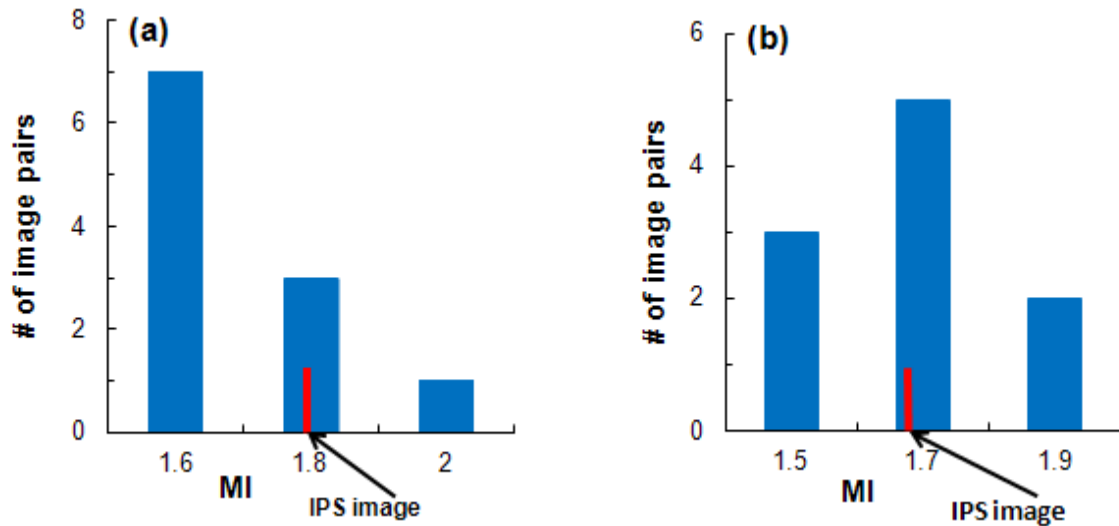


Figure 4.10: The MI index for (a) AP and (b) lateral projections of patient 4 (abdominal site) are shown. Histogram data correspond to the range of daily clinical images acquired using standard preset acquisition parameters. The MI values for the reduced-dose images are indicated by the red bars and were predicted by the IPS. See Table 4.3 for more information.

Table 4.3 summarizes the results of clinical data presented in Figures 4.9 and 4.10 and includes data for the other patients in our study. The data indicate that the MI index between the reference image and reduced-dose IPS image is within one standard deviation of the average MI for the typical daily images. These data support the assertion that there is no degradation in image contrast using the reduced-dose acquisition parameters derived using the IPS.

Table 4.3: MI between reference images versus images with presets and IPS parameters separately.

Patient	Site/projection	MI between reference image and images with preset parameters	MI between reference image and images with IPS parameters
1	Head/Neck, AP	2.30 ± 0.17	2.25
	Head/Neck, Lat	2.47 ± 0.20	2.23
2	Head/Neck, AP	2.31 ± 0.13	2.41
	Head/Neck, Lat	2.48 ± 0.18	2.43
3	Head/Neck, AP	2.27 ± 0.21	2.33
	Head/Neck, Lat	2.45 ± 0.11	2.47
4	Abdomen, AP	1.81 ± 0.18	1.84
	Abdomen, Lat	1.81 ± 0.15	1.82
5	Abdomen, AP	1.83 ± 0.14	1.76
	Abdomen, Lat	1.80 ± 0.22	1.79
6	Abdomen, AP	1.86 ± 0.12	1.88
	Abdomen, Lat	1.82 ± 0.11	1.74

4.4 Discussion

In its present state, the IPS algorithm calculates differences in attenuation based on density, but not atomic number. This is valid within the context of the proposed application of the algorithm. Photoelectric absorption scales as the cube of the atomic number Z , and inversely as the cube of the energy. Compton

scattering however is independent of Z and scales inversely with energy. Higher beam qualities will, therefore, result in less photoelectric and more Compton attenuation. Linac mounted x-rays systems, such as the one studied here, have a beam quality range of 40–150 kVp, and are most often used between 80 and 120 kVp. In this range, Compton processes dominate and attenuation coefficients are independent of atomic number for low and moderate atomic number materials. Consider that at 80 keV in bone, photoelectric processes account for approximately 15% of photon absorption, whereas Compton processes account for 85%.¹⁴³

Our results illuminate a counter-intuitive trend in which the visible image contrast appears to be independent of beam quality over the range tested (i.e., 80-120kVp). Initially, we assumed that by reducing the kVp setting we could affect an improvement in the contrast of the images, owing to the increase in photoelectric interactions. We tested this assumption using several phantoms, including an anthropomorphic phantom that contained human boney anatomy. Despite aggressively reducing the kVp to the lowest setting clinically available (i.e., 60kVp) we were not able to produce any improvement in boney or other tissue contrast that was clinically appreciable. In fact, the image quality was compromised due to the excessive noise introduced. To resolve this observation, we present a calculation demonstrating that, in a typical RT clinical scenario, beam hardening within the patient, and lack of penetration of low kVp spectral components, renders the low energy photoelectric interactions to be masked.

Consider the transmission of a hypothetical x-ray beam that has equal spectral components at 30, 50 and 100 keV. The attenuation through 20 cm of soft tissue and, separately, 20 cm of soft tissue plus 2 cm of bone are calculated using the x-ray mass attenuation coefficients for soft tissue and bone provided by the National Institutes of Standards and Technology (NIST).¹⁴⁴ The transmission through bone is calculated using two methods. The “full bone” method assumes a density of 1.92 g/cm³ and uses the energy-dependent attenuation coefficients for bone listed by NIST. The “water equivalent bone” method uses the proper density of bone (1.92 g/cm³) but uses the energy-dependent attenuation coefficients corresponding to soft tissue. The former method (full bone) is what would be expected to be the most accurate taking into account photoelectric interactions and full Z dependency. The latter method simulates our algorithm, which accounts for density and energy, but assumes mass attenuation properties for soft tissue. The contrast is calculated as

$$\text{Contrast} = (A-B)/A \quad (4.2)$$

where A is the sum of the net transmission components over all three energies through 20 cm soft tissue and B is the sum of net transmission components over all three energies through 20 cm soft tissue plus 2 cm bone.

Table 4.4: The transmitted intensity is calculated for equally weighted spectral components of a hypothetical x-ray beam. The “Full bone” calculations consider photoelectric interactions, whereas the “Water equivalent bone” calculations only consider Compton processes. The lack of transmission of the 30 and 50 keV components results in image contrast that is dominated by the 100 keV spectral component and Compton processes. The two calculation methods yield similar contrast at the exit of the hypothetical phantom.

	Spectral component			
	30 keV	50keV	100keV	
NIST data	$\frac{\mu}{\rho} \left(\frac{cm^2}{g} \right)$			density (g/cc)
Bone	1.330	0.424	0.186	1.92
Soft tissue	0.379	0.226	0.169	1
Transmission through individual phantom components				
20 cm soft tissue	0.001	0.011	0.034	
2 cm full bone	0.006	0.196	0.491	
2 cm water eq. bone	0.233	0.420	0.523	
Transmission through combined components				
Full bone	0.000	0.002	0.017	Soft tissue plus full bone
Water equivalent bone	0.000	0.005	0.018	Soft tissue plus water eq. bone
Fraction of all spectral components				
Full bone	0.000	0.113	0.886	
Water equivalent bone	0.005	0.203	0.791	
Net phantom contrast				
Full bone	0.59			
Water equivalent bone	0.51			

The results of this analysis are displayed in Table 4.4. Of note is that the 100 keV spectral component accounts for at least 79 % of the total transmitted

intensity, whereas the 30 keV component accounts for, at most, 0.5%. (See 'Fraction of all spectral components'). The net contrast for the full bone calculation is 59% and for water equivalent bone is 51%. So, indeed there will be some improvement in accuracy as we further develop the algorithm. However, in its current state, the clinically appreciable changes in contrast are driven by and adequately predicted by the limits of the detector response. This analysis also supports our observation that the peak kVp value (e.g., 80 kVp) is a good proxy for a heterogeneous, clinical x-ray beam.

We were very conservative in modifying image parameters in the clinical study and did not aggressively increase the recommended kVp for the purpose of reducing imaging dose.

The data presented herein are promising in that they demonstrate the system's ability to predict the following image characteristics:

- loss of contrast due to detector underexposure or saturation;
- maximum level of image contrast possible for a given imaging goal;
- the existence of a contrast plateau, sometimes over a wide latitude;
- reduction in imaging dose without appreciable loss of contrast;
- inability to improve contrast with changes in beam quality.

The existence of an image contrast plateau with respect to mAs setting may be intuitive, and we have shown that it can be quantitatively evaluated

prospectively via the IPS. This information has potential clinical value, in that the IPS can be used to select the image acquisition parameters that yield visibility of the objects of interest, or imaging goal, while reducing imaging dose. The data presented in Figures 4.6 and 4.7 show that the image contrast has a maximum value, and that this may be characterized as a broad plateau (Figure 4.6) or gradual peak (Figure 4.7). In both cases, mAs, or imaging dose, may be reduced such that contrast minimally exceeds that necessary to reveal the imaging goal, for example, boney anatomy. This mAs, or imaging dose level, does not necessarily yield the maximum contrast.

The potential for reducing imaging dose by using this patient-specific optimization technique is likely understated in the present study. In testing imaging parameters derived through use of the IPS, we chose to be very conservative in changing acquisition techniques from those prescribed by the vendor preset values. As such, any changes in acquisition parameters were incremental for this early clinical study, and likely do not exploit further reductions in dose that may be possible.

Use of the patient-specific CT data set renders the output of the image planning process to be patient-specific. This study could have a greater clinical impact in reducing imaging dose when applied to real-time image guidance, in which multiple frames per second^{145,146} are acquired for the duration of a treatment. In this clinical study, the areas we anticipate will require further development and testing include:

- resolution of the most appropriate handling of beam spectrum and hardening;
- incorporation of noise and scatter models; and
- change of clinical practice to higher kVp setting to see the possibility of more dose reduction.

4.5 Conclusions

The properties of the IPS algorithm were assessed with anthropomorphic and clinical data. The data and discussions presented in this chapter further confirm that image contrast resulting from under exposure, over exposure as well as a contrast plateau can be predicted by use of a prospective image planning algorithm. Image acquisition parameters can be predicted that reduce patient dose without loss of useful contrast.

CHAPTER 5: CONCLUDING REMARKS

5.1 Summary

Patient alignment is achieved by comparing kV planar images to DRRs created during the treatment planning process. While the DRRs are to some degree image simulations, they do not achieve the goal of image optimization or planning. To our knowledge, there is no commercial DRR reconstruction algorithm that allows the user to vary the x-ray spectrum (kVp), beam intensity (mAs) or acknowledges the detector response. In this work, I developed an IPS that can perform these tasks and hence can be used to assist in kV imaging technique selection during localization for radiotherapy. The patient-specific CT scan acquired during routine simulation was used as input. Detector response was incorporated into the algorithm and simulated images were generated by mapping the image intensity matrix reaching the detector.

Predictive accuracy of IPS

The predictive capability of the IPS was tested with different phantoms.

➤ High contrast / boney anatomy

Boney tissue contrast was studied using two abdominal phantoms, The incident exposure value (i.e., mAs value) for a given kVp at which detector saturation and subsequent loss of contrast occurs was predicted, as well as the invariance of the contrast at lower exposure settings.

Predictive accuracy was further verified quantitatively using the head/ neck, thorax/ abdomen and pelvis sites of an anthropomorphic phantom. MI was used to compare measured and simulated images acquired over a range of technique settings to a baseline image. The similarity between the MI index for the measured and simulated images was strong, over the wide latitude of technique settings tested.

Clinical verification was performed by using the IPS to predict reduced-dose imaging techniques which were then applied on one day of clinical image acquisition. Similarity between the revised image and standard images was established subjectively by human observers, and quantitatively by calculating the MI index. These methods demonstrated that no clinically appreciable change in boney anatomy contrast was observed using the revised acquisition parameters.

➤ Low contrast / soft tissue visualization

Mapping of the pixel intensity variation across a lung nodule test object of a respiratory motion phantom demonstrated the loss of contrast at low and high values of exposure (i.e. kVp and mAs) as well as the invariance of the contrast with exposure prior to detector saturation.

Similarly, mapping of the pixel intensity variation across a mammography step wedge phantom demonstrated agreement between measured and simulated images. Again, saturation, underexposure as well as small variations in grey scale value were correctly predicted by the IPS.

➤ Object detectability and geometric dimensions

Assessment of the lung nodule test object for its detectability, and geometric dimensions confirmed the IPS's ability to predict the loss of detectability and the reduction in visible dimension of the nodule at low and high values of exposure.

Dose reduction

➤ Selection of imaging goal

An anecdotal example supported the viability of using the IPS for selection of an imaging goal. The mammography step wedge phantom and high contrast fiducial marker were used to illustrate differences between imaging goals that are likely achievable or not.

➤ Reduction in ESE

Prospective selection of image acquisition parameters using the IPS was verified clinically. The results show that a 37% to 74% reduction in imaging dose is possible without loss of useful image contrast. This is a manifestation of the image contrast plateau observed over the course of multiple experiments contained within this study.

➤ Use of higher beam quality

Our results illuminated a counter-intuitive trend in which the visible image contrast appears to be independent of beam quality over the range tested, (i.e., 80-120kVp). Comparison of the MI index between a measured reference image and a range of simulated images using the pelvic region of the anthropomorphic phantom provided the subject contrast for these experiments.

These data suggest the potential of reducing imaging dose by selecting a high kVp without loss of useful image contrast.

5.2 Conclusions

Image contrast resulting from under exposure, over exposure as well as a contrast plateau can be predicted by use of an IPS. Patient specific image acquisition parameters can be predicted using the IPS that reduce patient dose without loss of contrast.

APPENDIX

A. 1 List of Abbreviations

ALARA:	As Low As Reasonably Achievable
AAPM:	American Association of Physicists in Medicine
AEC:	Automatic Exposure Control
aSi:	Amorphous Silicon
BEV:	Beam's Eye View
CBCT:	Cone Beam Computed Tomography
CNR:	Contrast to Noise Ratio
CT:	Computed Tomography
CTDI:	CT Dose Index
DAP:	Dose Area Product
DRR:	Digitally Reconstructed Radiograph
EBRT:	External Beam Radiation Therapy
EPID:	Electronic Portal Imaging Device
ESE:	Entrance Skin Exposure
FPD:	Flat Panel Detector
HU:	Hounsfield Units
ICRP:	International Commission on Radiological Protection
IGRT:	Image Guided Radiation Therapy
IMRT:	Intensity Modulated Radiation Therapy

IPS:	Image Planning System
kVD:	Kilovoltage Detector
kVS:	Kilovoltage Source
Linac:	Linear Accelerator
LNT:	Linear No Threshold
MI:	Mutual Information
MLC:	Multi Leaf Collimator
MV:	Megavoltage
NIST:	National Institutes of Standards and Technology
OAR:	Organ at Risk
OBI:	On Board Imager
QA:	Quality Assurance
ROI:	Region of Interest
RT :	Radiation Therapy
SBRT:	Stereotactic Body Radiation Therapy
SNR:	Signal to Noise ratio
SRS:	Stereotactic Radio Surgery
SSD	Source to Surface Distance
TFT:	Thin Film Transistor
TG:	Task Group
TLD:	Thermo Luminescence Dosimeter
TPS:	Treatment Planning System
VS:	Virtual Simulator

WW: Window Width

WL: Window Length

3-D CRT: Three Dimensional Conformal Radiation Therapy

BIBLIOGRAPHY

- ¹ M. Murphy et al., "The management of imaging dose during image-guided radiotherapy: Report of the AAPM Task Group 75," *Med. Phys.* 34, 4041–4063 (2007).
- ² J. D. Hosiak, K. E. Sixel, R. Tirona, P. C. Cheung, and J. P. Pigno, "Correlation of lung tumor motion with external surrogate indicators of respiration," *Int. J. Radiat. Oncol., Biol., Phys.* 60, 1298–1306 (2004).
- ³ D. Ionascu, S. B. Jiang, S. Nishioka, H. Shirato, and R. I. Berbeco, "Internal-external correlation investigations of respiratory induced motion of lung tumors," *Med. Phys.* 34, 3893–3903 (2007).
- ⁴ G. R. Baker, "Localization: conventional and CT simulation," *Br. J. Radiol.* 79, S36–S49 (2006).
- ⁵ E. G. A. Aird, and J. Conway, "CT simulation for radiotherapy treatment planning," *Br. J. Radiol.* 75, 937–949 (2002).
- ⁶ D. L. McShan, B. A. Fraass, and A.S. Lichter, "Full integration of the beam's eye-view concept into computerized treatment planning," *Int. J. Radiat. Oncol., Biol., Phys.* 18, 1485–1494 (1990).
- ⁷ G. J. Kutcher, L. Coia, M. Gillin, W. F. Hanson, S. Leibel, R. J. Morton, J. R. Palta, J. A. Purdy, L. E. Reinstein, G. K. Svensson, M. Weller, and L. Wingfield, "Comprehensive QA for radiation oncology: Report of the AAPM Radiation Therapy Committee Task Group 40," *Med. Phys.* 21, 581–618 (1994).
- ⁸ B. Fraass, K. Doppke, M. Hunt, G. Kutcher, G. Starkschall, R. Stern, and J. van Dyke, "Quality assurance for clinical radiotherapy planning. Report of AAPM Radiation Therapy Committee Task Group 53," *Med. Phys.* 25, 1773–1829 (1998).
- ⁹ J. H. Killoran, E. H. Baldini, C. J. Beard, and L. Chin, "A technique for optimization of digitally reconstructed radiographs of the chest in virtual simulation," *Int. J. Radiat. Oncol., Biol., Phys.* 49, 231–239 (2001).
- ¹⁰ J. M. Galvin, C. Sims, G. Dominiak, and J.S. Cooper, "The use of digitally reconstructed radiographs for three dimensional treatment planning and CT-simulation," *Int. J. Radiat. Oncol., Biol., Phys.* 31, 935–942 (1995).

-
- ¹¹ M. Y. Y. Law, "Dicom-RT and its utilization in radiation therapy," *RadioGraphics*. 29, 655–667 (2009).
- ¹² C. C. Ling, E. Yorke, Z. Fuks, "From IMRT to IGRT: Frontierland or Neverland?," *Radiother. Oncol.* 78, 119–122 (2006).
- ¹³ http://www.behestandarman.com/varian%20products/OBI/OBISpecs_RAD9502_H_March%202010.pdf
- ¹⁴ M. Spahn, "Flat detectors and their clinical applications," *Eur. Radiol.* 15, 1934–1947 (2005).
- ¹⁵ D. Jaffray et al., "Flat-panel conebeam tomography for image-guided radiation therapy," *Int. J. Radiat. Oncol., Biol., Phys.* 53, 1337–1349 (2002).
- ¹⁶ J. Seppi et al., "Megavoltage cone-beam computed tomography using a high-efficiency image receptor," *Int. J. Radiat. Oncol., Biol., Phys.* 55, 86–100 (2003).
- ¹⁷ M. J. Yaffe and J. A. Rowlands, "X-ray detectors for digital radiography" 1997 *Phys. Med. Biol.* 42, 1–39 (1997).
- ¹⁸ J. T. Bushberg, J. A. Seibert, E. M. Leidholdt, Jr., and J. M. Boone, *The Essential Physics of Medical Imaging*, 2nd ed. (Lippincott, Williams, and Wilkins. Philadelphia, 2002), pp. 330.
- ¹⁹ J. T. Bushberg, J. A. Seibert, E. M. Leidholdt, Jr., and J. M. Boone, *The Essential Physics of Medical Imaging*, 2nd ed. (Lippincott, Williams, and Wilkins. Philadelphia, 2002), pp. 356.
- ²⁰ T. G. Flohr, S. S. challer, K. Stierstorfer, H. Bruder, B. M. Ohnesorge, and U. J. Schoepf, "Multi-detector row CT systems and image reconstruction techniques" *Radiology* 235, 756–773 (2005).
- ²¹ L. W. Goldman, "Principles of CT: multislice CT," *J. Nuc. Med. Technol.* 36, 57–68 (2008).
- ²² G. Harding, "On the sensitivity and application possibilities of a novel Compton scatter imaging system," *IEEE Trans. Nucl. Sci.* 29, 1259–1265 (1982).
- ²³ C. M. Davisson, and R. D. Evans, "Gamma-ray absorption coefficients" *Rev. Mod. Phys.* 24, 79–107 (1952).
- ²⁴ F.H. Attix, *Introduction to Radiological Physics and Radiation Dosimetry*, (Wiley, New York, 1986), pp. 140.

-
- ²⁵ H. N. Cardinal, D. W. Holdsworth, M. Drangova, B. B. Hobbs, and A. Fenster, "Experimental and theoretical x-ray imaging performance comparison of iodine and lanthanide contrast agents," *Med. Phys.* 20, 15–31 (1993).
- ²⁶ M. Cuzin, "Some new developments in the field of high atomic number materials," *Nuc. Instrum. Methods Phys. Res.* 253, 407–417 (1987).
- ²⁷ F.H. Attix, *Introduction to Radiological Physics and Radiation Dosimetry*, (Wiley, New York, 1986), pp. 127.
- ²⁸ F.H. Attix, *Introduction to Radiological Physics and Radiation Dosimetry*, (Wiley, New York, 1986), pp. 127–129.
- ²⁹ J. T. Bushberg, J. A. Seibert, E. M. Leidholdt, Jr., and J. M. Boone, *The Essential Physics of Medical Imaging*, 2nd ed. (Lippincott, Williams, and Wilkins. Philadelphia, 2002), pp. 39–40.
- ³⁰ F.H. Attix, *Introduction to Radiological Physics and Radiation Dosimetry*, (Wiley, New York, 1986), pp. 127–129.
- ³¹ M.J. Gazda, and L.R. Coia, "Principles of Radiation Therapy," in: R. Pazdyr, L.R. Coia, W. J. Hoskins, L. D. Wagman, "Cancer Management: A Multidisciplinary Approach," 8th ed. (CMP, University of Michigan, 2004), pp. 9–21.
- ³² C. E. Webber, "The effect of fat on bone mineral measurements in normal subjects with recommended values of bone, muscle, and fat attenuation coefficients," *Clin. Phys. Physiol. Meas.* 8, 143–158 (1987).
- ³³ J. T. Bushberg, J. A. Seibert, E. M. Leidholdt, Jr., and J. M. Boone, *The Essential Physics of Medical Imaging*, 2nd ed. (Lippincott, Williams, and Wilkins. Philadelphia, 2002), pp. 44.
- ³⁴ F.H. Attix, *Introduction to Radiological Physics and Radiation Dosimetry*, (Wiley, New York, 1986), pp. 150.
- ³⁵ J. H. Hubbell, "Review and history of photon cross section Calculations," *Phys. Med. Biol.* 51, R245–R262 (2006)
- ³⁶ J. T. Bushberg, J. A. Seibert, E. M. Leidholdt, Jr., and J. M. Boone, *The Essential Physics of Medical Imaging*, 2nd ed. (Lippincott, Williams, and Wilkins. Philadelphia, 2002), pp. 37.
- ³⁷ F.H. Attix, *Introduction to Radiological Physics and Radiation Dosimetry*, (Wiley, New York, 1986), pp. 153.

-
- ³⁸ P. C. Johns and M. J. Yaffe, "Coherent scatter in diagnostic radiology," *Med. Phys.* 10, 40–50 (1983).
- ³⁹ F.H. Attix, *Introduction to Radiological Physics and Radiation Dosimetry*, (Wiley, New York, 1986), pp. 154.
- ⁴⁰ J. T. Bushberg, J. A. Seibert, E. M. Leidholdt, Jr., and J. M. Boone, *The Essential Physics of Medical Imaging*, 2nd ed. (Lippincott, Williams, and Wilkins. Philadelphia, 2002), pp. 45.
- ⁴¹ J.A. Seibert, and J. M. Boone, "X-ray imaging physics for nuclear medicine technologists. Part 2: X-ray interactions and image formation," *J. Nucl. Med. Technol.* 33, 3–18 (2005).
- ⁴² F.H. Attix, *Introduction to Radiological Physics and Radiation Dosimetry*, (Wiley, New York, 1986), pp. 141.
- ⁴³ <http://www.varian.com/media/xray/products/pdf/Flat%20Panel%20Xray%20Imaging%2011-11-04.pdf>
- ⁴⁴ J. A. Seibert, "Flat-panel detectors: how much better are they?," *Pediatr. Radiol.* 36, 173–181 (2006).
- ⁴⁵ J. T. Bushberg, J. A. Seibert, E. M. Leidholdt, Jr., and J. M. Boone, *The Essential Physics of Medical Imaging*, 2nd ed. (Lippincott, Williams, and Wilkins. Philadelphia, 2002), pp. 302.
- ⁴⁶ M. Spahn, "Flat detectors and their clinical applications," *Eur. J. Radiol.* 15, 1934–1947 (2005).
- ⁴⁷ Y. El-Mohri, L. E. Antonuk, J. Yorkston, K.-W. Jee, M. Maolinbay, K. L. Lam, and J. H. Siewerdsen, "Relative dosimetry using active matrix flat-panel imager (AMFPI) technology," *Med. Phys.* 26, 1530–1541 (1999).
- ⁴⁸ J. T. Bushberg, J. A. Seibert, E. M. Leidholdt, Jr., and J. M. Boone, *The Essential Physics of Medical Imaging*, 2nd ed. (Lippincott, Williams, and Wilkins. Philadelphia, 2002), pp. 301.
- ⁴⁹ <http://www.varian.com/media/xray/products/pdf/ps4030cb.pdf>
- ⁵⁰ National Council on Radiation Protection and Measurements, "Ionizing radiation exposure of the population of the United States," NCRP Report No. 160 (Bethesda, MD, 2009).
- ⁵¹ C. H. McCollough, and B. A. Schueler, "Calculation of effective dose," *Med. Phys.* 27, 828–837 (2000).

-
- ⁵² F. A. Mettler, W. Huda, T. T. Yoshizumi, and M. Mahesh, "Effective doses in radiology and diagnostic nuclear medicine: A catalog," *Radiology* 248, 254–63 (2008).
- ⁵³ National Radiological Protection Board. "X-rays: how safe are they?," Oxford, England: NRPB, 2001.
- ⁵⁴ C. H. McCollough et al., "Achieving routine submillisievert CT scanning: report from the Summit on Management of Radiation Dose in CT," *Radiology* 264, 567–580 (2012).
- ⁵⁵ M. T. Crawley, A. Booth, and A. Wainwright, "A practical approach to the first iteration in the optimization of radiation dose and image quality in CT: estimates of the collective dose savings achieved," *Br. J. Radiol.* 74, 607–614 (2001).
- ⁵⁶ D. J. Brenner, and E. J. Hall, "Computed tomography: an increasing source of radiation exposure," *N. Engl. J. Med.* 357, 2277–2284 (2007).
- ⁵⁷ G. D. D. Jones, T. V. Boswell, J. Lee, J. R. Milligan, J. F. Ward, and M. Weinfeld, "Comparison of DNA damages produced under conditions of direct and indirect action of radiation," *Int. J. Radiat. Biol.* 66, 441–445 (1994).
- ⁵⁸ E. J. Hall, *Radiobiology for the Radiologist*, 5th ed. (Lippincott Williams and Wilkins, Philadelphia, PA, 2000), pp.144–148.
- ⁵⁹ B. Nikolic, J. B. Spies, M. J. Lundsten, and S. Abbara, "Patient radiation dose associated with uterine artery embolization," *Radiology* 214, 121–125 (2000).
- ⁶⁰ R. J. Michael Fry, "Deterministic effects," *Health Phys.* 80, 338–343 (2001).
- ⁶¹ L. K. Wagner, P. J. Eifel, and R. A. Geise, "Potential biological effects following high x-ray dose interventional procedures," *J. Vasc. Interv. Radiol.* 5, 71–81 (1994).
- ⁶² National Council on Radiation Protection and Measurements, "Risk estimates for radiation protection," NCRP Report No. 148 (Bethesda, MD, 1993).
- ⁶³ A. Almen, and S. Mattsson, "On the calculation of effective dose to children and adolescents," *J. Radiol. Prot.* 16, 81–89 (1996).
- ⁶⁴ A. B. Wolbarst, *Physics of Radiology*, 2nd ed. (Medical Physics, Madison, 2000), pp. 554–556
- ⁶⁵ R. L. Brent, "Saving lives and changing family histories: appropriate counseling of pregnant women and men and women of reproductive age, concerning the risk

of diagnostic radiation exposures during and before pregnancy”, *Am. J. Obstet. Gynecol.* 200, 4–24 (2009).

⁶⁶ R. L. Brent, “Saving lives and changing family histories: appropriate counseling of pregnant women and men and women of reproductive age, concerning the risk of diagnostic radiation exposures during and before pregnancy”, *Am. J. Obstet. Gynecol.* 200, 4–24 (2009).

⁶⁷ E. C. Lin, “Radiation Risk From Medical Imaging,” *Mayo. Clin. Proc.* 85, 1142–1146, (2010).

⁶⁸ International Commission on Radiological Protection. “Pregnancy and medical radiation,” *ICRP Publication 84. Ann ICRP* 2000, 3–41.

⁶⁹ J. M. Boone, T. R. Nelson, K. K. Lindfors, and J. A. Seibert, “Dedicated breast CT: radiation dose and image quality evaluation,” *Radiology* 221, 657–667 (2001).

⁷⁰ N. A. Gkanatsios, W. Huda, and K. R. Peter, “Effects of radiographic techniques (kVp and mAs) on image quality and patient doses in digital subtraction angiography,” *Med. Phys.* 29, 1643–1650 (2002).

⁷¹ W. Huda, J. G. Ravenel, and E. M. Scalzetti, “How do radiographic techniques affect image quality and patient doses in CT?,” *Semin Ultrasound CT MR* 23, 411–422 (2002).

⁷² T. R. Fewell and R. E. Shuping, “Photon energy distribution of some typical diagnostic x-ray beams,” *Med. Phys.* 4, 187–97 (1977).

⁷³ J.T. Bushberg, “The AAPM/RSNA physics tutorial for residents: X-ray interactions” *RadioGraphics* 18, 457–468 (1977).

⁷⁴ P. R. Granfors, “Performance characteristics of an amorphous silicon flat panel x-ray imaging detector,” *Proc. SPIE* 3659, 480–490 (1999).

⁷⁵ A. Paterson, and D. P. Frush, “Dose reduction in paediatric MDCT: general principles,” *Clin. Radiol.* 62, 507–517 (2007).

⁷⁶ A. E. Robinson, E. P. Hill, and M.D. Harpen, “Radiation dose reduction in pediatric CT,” *Pediatr. Radiol.* 16, 53–54 (1986).

⁷⁷ C. E. Willis, “Strategies for dose reduction in ordinary radiographic examinations using CR and DR,” *Pediatr. Radiol.* 34 (suppl3), S196–S200 (2004).

-
- ⁷⁸ J. R. Mayo, and J. A. Leipsic, "Radiation dose in cardiac CT," *AJR, Am. J. Roentgenol.* 192, 646–653 (2009).
- ⁷⁹ C. H. McCollough, A. N. Primak, N. Braun, J. Kofler, L. Yu, and J. Chistner, "Strategies for reducing radiation dose in CT," *Radiol. Clin. North. Am.* 47, 27–40 (2009).
- ⁸⁰ R. Fazel et al., "Exposure to low-dose ionizing radiation from medical imaging procedures," *N. Engl. J. Med.* 361, 849–857 (2009).
- ⁸¹ L. Yu et al., "Radiation dose reduction in computed tomography: techniques and future perspective," *Imaging Med.* 1, 65–84 (2009).
- ⁸² S. Green, and E. Aird, "Imaging in radiotherapy," *Br. J. Radiol.* 80, 967–969 (2007).
- ⁸³ O. Morin, A. Gillis, M. Descovich, J. Chen, and M. Aubin, "Patient dose considerations for routine megavoltage cone-beam CT imaging," *Med. Phys.* 34, 1819–1827 (2007).
- ⁸⁴ C. W. Coffey et al., "AAPM protocol for 40–300 kV x-ray beam dosimetry in radiotherapy and radiobiology," *Med. Phys.* 28, 868–893 (2001).
- ⁸⁵ M. C. Aznar et al., "In vivo absorbed dose measurements in mammography using a new real-time luminescence technique" *Br. J. Radiol.* 78, 328–34 (2005).
- ⁸⁶ J. M. Boone, E. M. Geraghty, J. A. Seibert, and S. L. Wootton-Gorges, "Dose reduction in pediatric CT: a rational approach," *Radiology*, 228, 352–360 (2003).
- ⁸⁷ M. F. McNitt-Gray, "AAPM/RSNA physics tutorial for residents—topics in CT: radiation dose in CT," *Radiographics* 22, 1541–1553 (2002).
- ⁸⁸ F. M. Khan, *The Physics of Radiation Therapy*, 4th ed. (Lippincott Williams & Wilkins, Philadelphia, 2010), pp. 510.
- ⁸⁹ A.J. Einstein, K.W. Moser, R.C. Thompson, M.D. Cerqueira, and M.J. Henzlova, "Radiation dose to patients from cardiac diagnostic imaging," *Circulation.* 116, 1290-1305 (2007).
- ⁹⁰ T. R. C. Johnson et. al., "Material differentiation by dual energy CT: initial experience," *Eur. Radiol.* 17, 1510–1517 (2007).
- ⁹¹ L. W. Goldman, "Principles of CT: radiation dose and image quality," *J. Nucl. Med. Technol.* 35, 213–225 (2007).

-
- ⁹² L. K. Wagner, P. J. Eifel, and R. A. Geise, "Potential biological effects following high x-ray dose interventional procedures," *J. Vasc. Interv. Radiol.*, 5, 71–81 (1994).
- ⁹³ F. A. Mettler, W. Huda, T. Y. Terry, and M. Mahesh, "Effective doses in radiology and diagnostic nuclear medicine: a catalog," *Radiology*, 248 (1), (2008).
- ⁹⁴ W. Huda, and N. A. Gkanatsios, "Effective dose and energy imparted in diagnostic radiology," *Med. Phys.* 24 (8), (1997).
- ⁹⁵ W. Jacobi, "The concept of effective dose: A proposal for the combination of organ doses," *J. Radiat. Environ. Biophys.* 12, 101–109, (1975).
- ⁹⁶ C. H. McCollough, and B. A. Schueler, "Calculation of effective dose: educational treatise," *Med. Phys.* 27, 828–837 (2000).
- ⁹⁷ The International Commission on Radiological Protection, *Recommendations on Radiation Protection*, ICRP Publication 60 (Pergamon Press, Oxford, 1991).
- ⁹⁸ D. Hart, D. G. Jones, and D. F. Wall, *Estimation of effective dose in diagnostic radiology from entrance surface dose and dose–area product measurements*, NRPB R-262 (National Radiological Protection Board, Oxon 1994).
- ⁹⁹ R. L. Morin, T. C. Gerber, and C. H. McCollough, "Radiation dose in computed tomography of the heart," *Circulation* 107, 917-922 (2003).
- ¹⁰⁰ J. C. Le Heron, "Estimation of effective dose to the patient during medical x-ray examinations from measurements of the dose-area product," *Phys. Med. Biol.* 37, 2117–2126 (1992).
- ¹⁰¹ C. J. Martin, D. G. Sutton, and P. F. Sharp, "Balancing patient dose and image quality," *Appl. Radiat. Iso.* 50, 1–19 (1999).
- ¹⁰² C. C. Chamberlain, W. Huda, L. S. Hojnowski, A. Perkins, and A. Scaramuzzino, "Radiation doses to patients undergoing scoliosis radiography," *Br. J. Radiol.* 73, 847–853 (2000).
- ¹⁰³ H. A. Omran, "Thermoluminescent dosimeters for in vivo measurement of radiation exposure and related dose in mammography," *Radiol. Technol.* 53, 383–392 (1982).
- ¹⁰⁴ H. M. Warren-Forward, and L. Duggan, "Towards in vivo TLD dosimetry in mammography," *Br. J. Radiol.* 77, 426–432 (2004).

-
- ¹⁰⁵ B. J. McParland, "A study of patient radiation doses in interventional radiological procedures," *Br. J. Radiol.* 71, 175–185 (1998).
- ¹⁰⁶ B. M. Moores, "Radiation dose measurement and optimization," *Br. J. Radiol.* 78, 866–868 (2005).
- ¹⁰⁷ A. Kraskov, and H. Stogbauer, and P. Grassberger, "Estimating mutual information," *Phys. Rev. E* 69, 019903 (2004).
- ¹⁰⁸ V. Roshni, and D. Revathy, "Using mutual information and cross correlation as metrics for registration of images," *J. Theor. Appl. Inf. Technol.* 4, 474-481 (2008).
- ¹⁰⁹ R. Steuer, J. Kurths, C.O. Daub, J. Weise, and J. Selbig, "The mutual information: detecting and evaluating dependencies between variables," *Bioinformatics* 18 (Suppl 2), 231–240, *Evaluation Stud* (2002).
- ¹¹⁰ B. F. Hutton, and M. Braun, "Software for image registration: algorithms, accuracy, efficacy," *Semin. Nucl. Med.* 33, 180–192 (2003).
- ¹¹¹ T. M. Cover and J. A. Thomas, *Elements of Information Theory*. 2nd ed. (Wiley, New York, 1991), pp.12-20.
- ¹¹² F. Maes, A. Collignon, D. Vandermeulen, G. Marchal, and P. Suetens, "Multimodality image registration by maximization of mutual information," *IEEE Trans. Med. Imag.* 16, 187–198 (1997).
- ¹¹³ J. P. W. Pluim, J. B. A. Maintz, and M. A. Viergever, "Mutual-information based registration of medical images: a survey," *IEEE Trans. Med. Imag.* 22, 986–1004, (2003).
- ¹¹⁴ F. Maes, D. Vandermeulen, P. Suetens, "Medical image registration using mutual information," *Proceedings of the IEEE*, 91, 1699-1722 (2003).
- ¹¹⁵ D. B. Russakoff, C. Tomasi, T. Rohlfing, and C. R. Maurer, Jr., "Image similarity using mutual information of regions," in *Lecture Notes in Computer Science*, edited by T. Pajdla and J. Matas (Springer, Berlin 2004), Vol. 3023, *ECCV 2004*, pp. 596–607.
- ¹¹⁶ E. L. Chaney et al., "A portable software tool for computing digitally reconstructed radiographs," *Int. J. Radiat. Oncol., Biol., Phys.* 32, 491–497 (1995).

-
- ¹¹⁷ J. M. Galvin, C. Sims, G. Dominiak, and J. S. Cooper, "The use of digitally reconstructed radiographs for three dimensional treatment planning and CT-simulation," *Int. J. Radiat. Oncol., Biol., Phys.* 31, 935–942 (1995).
- ¹¹⁸ J. H. Killoran, E. H. Baldini, C. J. Beard, and L. Chin, "A technique for optimization of digitally reconstructed radiographs of the chest in virtual simulation," *Int. J. Radiat. Oncol., Biol., Phys.* 49, 231–239 (2001).
- ¹¹⁹ J. T. Bushberg, J. A. Seibert, E. M. Leidholdt, Jr., and J. M. Boone, *The Essential Physics of Medical Imaging*, 2nd ed. (Lippincott, Williams, and Wilkins. Philadelphia, 2002), pp. 204–206.
- ¹²⁰ E. D. Pisano, M. J. Yaffe, "Digital Mammography," *Radiology* 234, 353–362 (2005).
- ¹²¹ I. A. Elbakri, A. V. Lakshminarayanan, and M. M. Tesic, "Automatic exposure control for a slot scanning full field digital mammography system," *Med. Phys.* 32, 2763–2770 (2005).
- ¹²² M. Varjonen, and P. Strömmer, "Anatomically adaptable automatic exposure control (AEC) for amorphous selenium (aSe) full field digital mammography (FFDM) system," *Proc SPIE*, 6142: 614207 (2006).
- ¹²³ H. P. Chan and K. Doi, "Radiation dose in diagnostic radiology: Monte Carlo simulation studies," *Med. Phys.* 11, 480–490 (1984).
- ¹²⁴ H. Yoriyaz, M. G. Stabin, and A. dos Santos, "Monte Carlo MCNP-4B-based absorbed dose distribution estimates for patient-specific dosimetry," *J. Nucl. Med.* 42, 662–669 (2001).
- ¹²⁵ G. Jarry, J. J. DeMarco, U. Beifuss, C. H. Cagnon, and M. F. McNitt-Gray, "A Monte Carlo-based method to estimate radiation dose from spiral CT: from phantom testing to patient specific models," *Phys. Med. Biol.* 48, 2645–63 (2003).
- ¹²⁶ P. Deak, M. van Straten, P. C. Shrimpton, M. Zankl , and W. Kalender, "Validation of a Monte Carlo tool for patient-specific dose simulations in multi-slice computed tomography," *Eur. Radiol.* 18, 759–772(2008).
- ¹²⁷ X. Jia, H. Yan, X. Gu and S. B. Jiang, "Fast Monte Carlo simulation for patient-specific CT/CBCT imaging dose calculation," *Phys. Med. Biol.* 57, 577–590 (2012).

-
- ¹²⁸ J. V. Siebers, J. O. Kim, L. Ko, P. J. Keall, and R. Mohan, "Monte Carlo computation of dosimetric amorphous silicon electronic portal images," *Med. Phys.* 31, 2135–2146 (2004).
- ¹²⁹ S. Li, J. Li, B. Yan, Y. Liu, and L. Li, "The Monte Carlo simulation of CT based on Flat Panel Detector," 2011 4th International Congress on Image and Signal Processing, 2798–2801 (2011).
- ¹³⁰ L. Parent, J. Seco, P. M. Evans, A. Fielding, and D. R. Dance, "Monte Carlo modelling of a-Si EPID response: The effect of spectral variations with field size and position," *Med. Phys.* 33, 4527–4540, (2006).
- ¹³¹ B. J. Mcparland, "Entrance skin dose estimates derived from dose area product measurements in interventional radiological procedures," *Br. J. Radiol.* 71, 1288–1295 (1998).
- ¹³² T. B. Shope, "Radiation-induced skin injuries from fluoroscopy," *Radiographics* 16, 1195–1199 (1996).
- ¹³³ K. Chida et. al., "Total Entrance Skin Dose: An Effective Indicator of Maximum Radiation Dose to the Skin During Percutaneous Coronary Intervention," *Am. J. Roentgenol.* 189, W224–W227 (2007).
- ¹³⁴ G. Poludniowski, G. Landry, F. DeBlois, P. M. Evans, and F. Verhaegen, "SpekCalc: a program to calculate photon spectra from tungsten anode x-ray tubes," *Phys. Med. Biol.* 54, N433–N438 (2009).
- ¹³⁵ Y. Lin, H. Luo, and J. T. Dobbins, "An image-based technique to assess the perceptual quality of clinical chest radiographs," *Med. Phys.* 39, 7019–7031(2012).
- ¹³⁶ W. Morrow, R. Paranjape, R. Rangayyan, and J. Desautels, "Region-based contrast enhancement of mammograms," *IEEE Trans. Med. Imag.* 11, 392–406 (1992).
- ¹³⁷ H. D. Cheng, X. J. Shi, R. Min, L. M. Hu, X. P. Cai, and H. N. Du, "Approaches for automated detection and classification of masses in mammograms," *Pattern Recognit.* 39, 646–668 (2006).
- ¹³⁸ B. Thapa, and J. Molloy, "Feasibility of an image planning system for kilo-voltage image-guided radiation therapy," *Med. Phys.* 40, 061303(1)-061703(14), (2013).

-
- ¹³⁹ D. A. Jaffray, "Kilovoltage volumetric imaging in the treatment room," *Front. Radiat. Ther. Oncol.* 40, 116–131 (2007).
- ¹⁴⁰ J. Pouliot *et al.*, "Low-dose megavoltage cone-beam CT for radiation therapy," *Int. J. Radiat. Oncol., Biol., Phys.* 61, 552–560 (2005).
- ¹⁴¹ J. T. Bushberg, J. A. Seibert, E. M. Leidholdt, Jr., and J. M. Boone, *The Essential Physics of Medical Imaging*, 2nd ed. (Lippincott, Williams, and Wilkins. Philadelphia, 2002), pp. 802–805.
- ¹⁴² C. J. Tung, and H. Y. Tsai, "Evaluations of Gonad and Fetal Doses for Diagnostic Radiology," *Proc. Natl. Sci. Counc. ROC(B)*, 23, 107–113 (1999).
- ¹⁴³ J. T. Bushberg, J. A. Seibert, E. M. Leidholdt, Jr., and J. M. Boone, *The Essential Physics of Medical Imaging*, 2nd ed. (Lippincott, Williams, and Wilkins. Philadelphia, 2002), pp. 43.
- ¹⁴⁴ J. H. Hubbell and S. M. Seltzer, *Tables of X-Ray Mass Attenuation Coefficients and Mass Energy-Absorption Coefficients from 1keV to 20MeV for Elements Z=1 to 92 and 48 Additional Substances of Dosimetric Interest*, NISTIR 5632 (US Secretary of Commerce, 1996).
- ¹⁴⁵ T. Bortfeld and G. Chen, "High precision radiation therapy of moving targets," *Semin. Radiat. Oncol.* 14, 1–100 (2004).
- ¹⁴⁶ M. J. Murphy, "Tracking moving organs in real time," *Semin. Radiat. Oncol.* 14, 91–100 (2004).

VITA

Bishnu Bahadur Thapa

Place of birth:

Hemja V.D.C-2, Kaski, Nepal

Educational institutions attended and degrees awarded:

- 2007 - 2013: PhD, Department of Physics and Astronomy,
University of Kentucky, KY, USA (expected
graduation in 2013)
- 2011 - Present: M.S., Radiological Medical Physics, University of
Kentucky, KY, USA (expected graduation in 2013)
- 2007 – 2010: M.S., Department of Physics and Astronomy,
University of Kentucky, KY, USA, 2010
- 2001 – 2004: Master of Science (M.Sc.) in Physics, Tribhuvan
University, Nepal, 2004

- 1998 – 2001: Bachelor of Science (B.Sc.) in Physics, Tribhuvan University, Nepal, 2001

Professional positions held:

- 2010 – 2013: Graduate Research Assistant at University of Kentucky, Department of Radiation Medicine, KY, USA
- 2007 – 2010: Graduate Teaching Assistant at University of Kentucky, Department of Physics, KY, USA
- 2005 – 2007: Physics Lecturer at Prithvi Narayan Multiple Campus; Janapriya Multiple Campus; Novel Academy; Cosmos International College; Pokhara, Nepal

Professional publications:

1. **B. Thapa**, and J. Molloy, “Feasibility of an image planning system for kilovoltage image-guided radiation therapy,” Med. Phys. 40, 061303(1)-061703(14), (2013).
2. **B. Thapa**, J. Zhang, and J. Molloy, “Prospective image planning in radiation therapy for optimization of image quality and reduction of patient dose,” (Submitted to Medical Physics Journal)

Published abstracts:

1. **B. Thapa**, J. Molloy, “Prospective Image Planning in Radiation Therapy for Optimization of Image Quality and Reduction of Patient Dose”, Accepted for Oral presentation at the 55th Annual Meeting of the American Association of Physicists in Medicine (AAPM), Indianapolis, IN; August 04- August 08, 2013.
2. **B. Thapa**, J. Molloy, “Development of Image Planning System for Radiation Therapy”, Poster presentation at the 54th Annual Meeting of the American Association of Physicists in Medicine (AAPM), Charlotte, NC; July 29- Aug 02, 2012, SU-E-J-178, Medical Physics, Vol. 39, No.6, Page 3693 (2012).
3. J. Molloy, **B. Thapa**, “Feasibility of a Quantitative, Patient-Specific Image Planning System for Radiation Therapy” Poster presentation at the 53rd Annual Meeting of the American Association of Physicists in Medicine (AAPM) and 2011 Joint AAPM/COMP meeting, Vancouver, B. C., Canada; July 31- Aug 04, 2011, SU-E-J-103, Medical Physics, Vol. 38, No.6, Page 3466 (2011).